BRNO UNIVERSITY OF TECHNOLOGY
VYSOKÉ UČENÍ TECHNICKÉ V BRNĚ

FACULTY OF MECHANICAL ENGINEERING
FAKULTA STROJNÍHO INŽENÝRSTVÍ

INSTITUTE OF PHYSICAL ENGINEERING
ÚSTAV FYZIKÁLNÍHO INŽENÝRSTVÍ

ARTIFICIAL SHAKTI ICE MAGNETS: GROUND STATE DEGENERACY, COULOMB PHASE AND MONOPOLE EXCITATIONS
UMĚLÉ MAGNETY LEDU SHAKTI: DEGENERACE ZÁKLADNÍHO STAVU, COULOMBOVA FÁZE A MONOPÓLOVÉ EXCITACE

MASTER'S THESIS
DIPLOMOVÁ PRÁCE

AUTHOR
AUTOR PRÁCE

Bc. Marek Zálešák

SUPERVISOR
VEDOUCÍ PRÁCE

Nicolas Rougemaille

BRNO 2023

Assignment Master's Thesis

Institut: Institute of Physical Engineering
Student: **Bc. Marek Zálešák**
Degree programm: Physical Engineering and Nanotechnology
Branch: no specialisation
Supervisor: **Nicolas Rougemaille**
Academic year: 2022/23

As provided for by the Act No. 111/98 Coll. on higher education institutions and the BUT Study and Examination Regulations, the director of the Institute hereby assigns the following topic of Master's Thesis:

Artificial Shakti ice magnets:
ground state degeneracy, Coulomb phase and monopole excitations

Brief Description:

Exploring artificial spin ice systems is a way how to investigate phenomena and interesting physics in nature which are challenging to observe directly. Interaction of nanomagnets set in artificial arrays can simulate the behaviour of such matter. These magnetic systems allow us to directly observe behaviour typical for low–energy physics such as Classical spin liquids, emerging magnetic properties, Coulomb phases and complex magnetic ordering.

This work is focused on Shakti geometry which can provide means to address the physics of the square ice, but in an emergent form. In this Master thesis, we aim at going a step further in the understanding of the Shakti properties. Combining magnetic imaging performed on lithographically made arrays and Monte Carlo simulations, we will investigate in more detail the analogy proposed in the literature between the Shakti ice and the square ice.

Master's Thesis goals:

1. Review the state–of–the–art.
2. Investigate the analogy proposed in the literature between the Shatki ice and the square ice by combining Monte Carlo simulations and magnetic imaging performed on lithographically made arrays.
3. Determine whether Shakti ice magnets host a Coulomb phase physics and monopole–like excitations, like in the seminal square ice model.

Recommended bibliography:

GILBERT, Ian, Gia-Wei CHERN, Sheng ZHANG, Liam O'BRIEN, Bryce FORE, Cristiano NISOLI a Peter SCHIFFER. Emergent ice rule and magnetic charge screening from vertex frustration in artificial spin ice. Nature Physics [online]. 2014, 10(9), 670-675. Dostupné z: doi:10.1038/nphys3037

CHERN, Gia-Wei, Muir J. MORRISON a Cristiano NISOLI. Degeneracy and Criticality from Emergent Frustration in Artificial Spin Ice. Physical Review Letters [online]. 2013, 111(17). Dostupné z: doi:10.1103/PhysRevLett.111.177201

ROUGEMAILLE, Nicolas a Benjamin CANALS. Cooperative magnetic phenomena in artificial spin systems: spin liquids, Coulomb phase and fragmentation of magnetism – a colloquium. The European Physical Journal B [online]. 2019, 92(3). Dostupné z: doi:10.1140/epjb/e2018-90346-7

Deadline for submission Master's Thesis is given by the Schedule of the Academic year 2022/23

In Brno,

L. S.

_____   _____
prof. RNDr. Tomáš Šikola, CSc.   doc. Ing. Jiří Hlinka, Ph.D.
Director of the Institute   FME dean

ABSTRACT

Artificial spin systems have emerged as a promising platform for studying in real space and harnessing exotic states of matter. This diploma thesis investigates the unique properties of a specific artificial spin system known as the shakti ice magnet. The shakti ice magnet is a two-dimensional arrangement of interacting nano-magnets, exhibiting intriguing magnetic behaviour.

This research aimed at characterising its behaviour and its ability to be mapped onto the seminal square ice in which interesting Coulomb physics is expected. A combination of experimental measurements and numerical simulations was employed to achieve these objectives. Experiments were based on MFM measurements to determine the magnetic configuration of samples containing lithographically prepared shakti lattices.

KEYWORDS

artificial spin systems, artificial magnetic spin systems, shakti lattice, vertex model, magnetic force microscopy, spin dynamics, Coulomb phase.

ABSTRAKT

Umělé spinové systémy se staly slibnou platformou pro studium nízkoenergetických stavů v reálném prostoru. Tato diplomová práce zkoumá jedinečné vlastnosti specifického umělého spinového systému známého jako ledový magnet shakti. Ledový magnet shakti je dvourozměrné uspořádání interagujících nano-magnetů, projevujících zajímavé magnetické chování.

Tato studie si klade za cíl charakterizovat chování ledového magnetu shakti a jeho schopnost být mapován na fundamentální čtvercový spinový led, kde se očekává projevení zajímavé Coulombovské fyziky. K dosažení těchto cílů byla využita kombinace experimentálních měření a numerických simulací. Experimenty byly založeny na měření magnetické silové mikroskopie pro stanovení magnetické konfigurace vzorků obsahující litograficky připravené shakti mřížky.

KLÍČOVÁ SLOVA

umělý spinový systém, umělý magnetický spinový systém, mřížka shakti, vertexový model, mikroskopie magnetických sil, spinový dynamika, Coulombova fáze.

Author's Declaration

Author:	Bc. Marek Zálešák
Author's ID:	209502
Paper type:	Master's Thesis
Academic year:	2022/23
Topic:	Artificial Shakti ice magnets: ground state degeneracy, Coulomb phase and monopole excitations

I declare that I have written this paper independently, under the guidance of the supervisor and using exclusively the technical references and other sources of information cited in the paper and listed in the comprehensive bibliography at the end of the paper.

Brno . . . .
author's signature*

---

*The author signs only in the printed version.

ACKNOWLEDGEMENT

Bc. Marek Zálešák

Contents

1　Introduction

In this work, I focused on a special area of condensed matter physics consisting of the analysis of artificial frustrated spin systems. The phenomenon of frustration, such as frustration in water ice between oxygen and hydrogen atoms, has led scientists to develop other approaches to studying the properties of this exotic physics. For this purpose, artificial magnetic systems have been developed that mimic this phenomenon observed in nature. Frustration in the system is meditated by magnetic interactions between nanomagnets produced by lithographic techniques.

These nano-magnets can be arranged in different geometries that provide different system properties and behaviour. The work on my diploma thesis consisted of exploring several geometries with an emphasis on the situation where nanomagnets are placed on a shakti lattice.

In these systems, it is possible to observe an interesting physics. When several conditions are met, the system can be in the lowest energy state, the ground state, and at the same time, it can be disordered. When the system is in this exotic state, we can call it a spin-liquid or Coulomb phase. Just above the ground state, when excitations begin to appear, another phenomenon can be studied. Under these conditions, the excitations will behave like electrostatically charged free particles. These excitations, also called monopoles for their charge properties, interact as positively or negatively charged Coulomb-like particles. They can repel or attract each other, but their origin is not electrostatic but purely magnetic.

In recent years, scientific work on the shakti lattice has been published and created another branch of frustrated magnetic systems. In a theoretical article, Chern et al. describe a very interesting connection between the ground state of the shakti lattice and a spin-liquid phase on a square lattice. In another publication, Gilbert et al. confirm this theory experimentally and claims that the disordered state of spin-liquid can be observed even above the ground state.

The goal of this work is to carefully reanalyse the experiments done by Gilbert et al. with a new approach and study the ice physics in the shakti lattice. Also, no magnetic monopoles were mentioned in the previous works that are inextricably linked with the Coulomb phase. The physics of monopoles and their impact on the whole shakti system will be presented.

2 Scientific background

2.1 Frustrated systems in nature

Frustration is a natural feature of many systems in nature. These systems are not able to satisfy all interactions at the same time [18]. The history of frustrated systems dates back to the 1930s when physicists attempted to clarify the non-zero entropy of water ice at cryogenic temperatures [13]. In 1935, Linus Pauling came up with a model describing these findings [29]. According to this model, the oxygen atom is surrounded by four hydrogens, where two hydrogens are bound to oxygen by a stronger bond than the other two hydrogens. This results in a situation where two hydrogens are always closer to the oxygen and two further away. The schematic of this atom arrangement can be seen in figure 2.1.
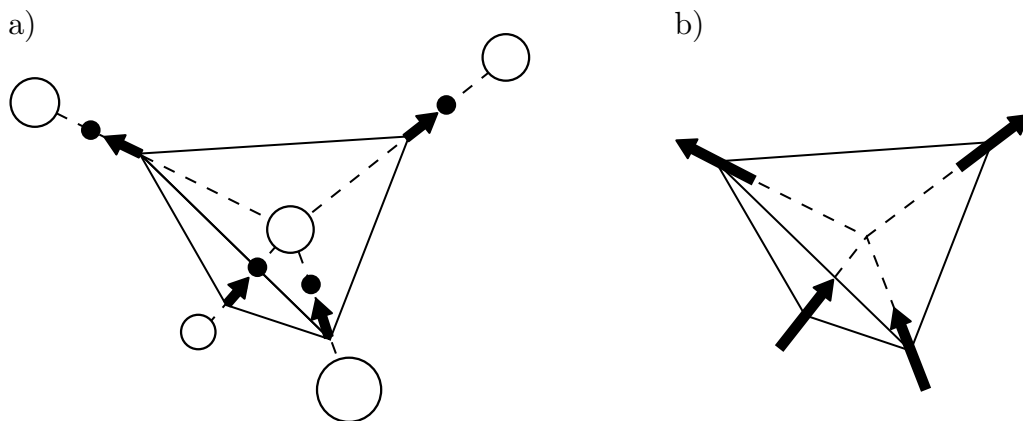

Fig. 2.1: a) Schematic of a water molecule in the tetrahedral coordination of the ice structure. Oxides are depicted by open circles and protons by filled circles. The position of the proton is located by displacement vectors that occupy a lattice of linked tetrahedra. b) In spine ice the displacement vectors are replaced by Ising spins occupying the pyrochlore lattice. Adapted from [4].

One can imagine that the position of these hydrogen atoms can be expressed by an arrow (or by a spin) where the close proximity of the hydrogen near the oxygen atom corresponds to the head of the arrow and the more distant hydrogen corresponds to the tail of the arrow. Now a problem of the position is transferred to a spin model problem. During the second half of the 20th century, several two-dimensional models were introduced and solved by Lieb [19]. Now it is more appropriate to talk about vertex models because these models fully describe the whole system [1].

In 1997, Harris introduced other materials where frustration also occurs. These materials, such as $Ho_2Ti_2O_7$ [15] and $Dy_2Ti_2O_7$ [5], are rare-earth materials with the same ice model able to describe the physics of the atomic magnetic moments in these compounds as in water ice and its hydrogen positions. However, this approach could not provide information about each magnetic moment orientation, but only the overall results of the bulk sample. This and other disadvantages led to a new

branch of frustrated systems studies where local information and easier measurement processes were present.

2.2 Frustrated artificial systems

For the purpose of approaching these exotic systems, artificial magnetic systems have been developed. Frustration in the system is meditated by magnetic interactions between nano-magnets produced by lithographic techniques [39]. These nano-magnets can be arranged in several geometries that provide different system properties and behaviours. By tuning these parameters, one can design the system properties and probe these systems with a lab-on-chip approach.

In the beginning, the water ice structure has been the inspiration for geometries in artificial systems. Hydrogen atoms and their position between two oxygen atoms in water ice at low-temperature form a tetrahedral lattice with shared corners. By projecting corner-shared tetrahedral lattice in a plane one can obtain two fundamental geometries used in frustrated artificial systems - the square lattice [24] and the kagome lattice.

These two geometries differ especially in their coordination number, i.e. by the number of nano-magnets that interact in a single vertex and their orientation in a lattice. In a classical square lattice, the interaction is among four magnets (coordination number is $z = 4$) and in a kagome lattice is among three magnets (coordination number is $z = 3$). In this thesis, more focus will be on a classical square lattice which is fundamental for other geometry called shakti.

2.3 Classical square lattice

One of the most basic geometric arrangements is a classical square lattice (CSL). In this geometry, one can observe competition between the coupling strengths when the interactions between the first and second neighbours are ferromagnetic. This kind of system can be described by a vertex model, which was theoretically solved for specific cases by Lieb [19, 20, 21].

In this case, the coupling strength is provided by magnetostatic interaction between nano-magnets fabricated of permalloy which are single domains [39, 40]. Thus we can assign for such a magnet an orientation of its magnetization which we depict as a pseudo-spin (or an Ising variable). This nano-magnet is creating a magnetic stray field that can affect other magnets in its surrounding. In figure 2.2b one can see four nano-magnets in a square geometry and their spins that are aligned with the stray field coming out of the first magnet on the left side of the figure. From the point of view of the first magnet, the other ones are aligned and the system is in the lowest energy. But considering other nano-magnets one can see that just one nano-magnet is aligned with its stray field but the other two magnetizations are in opposite directions. In this organization, the system is frustrated and the lowest energy of the vertex must be a compromise among all the magnets. How this compromise will look like will be dependent on the coupling strength between the
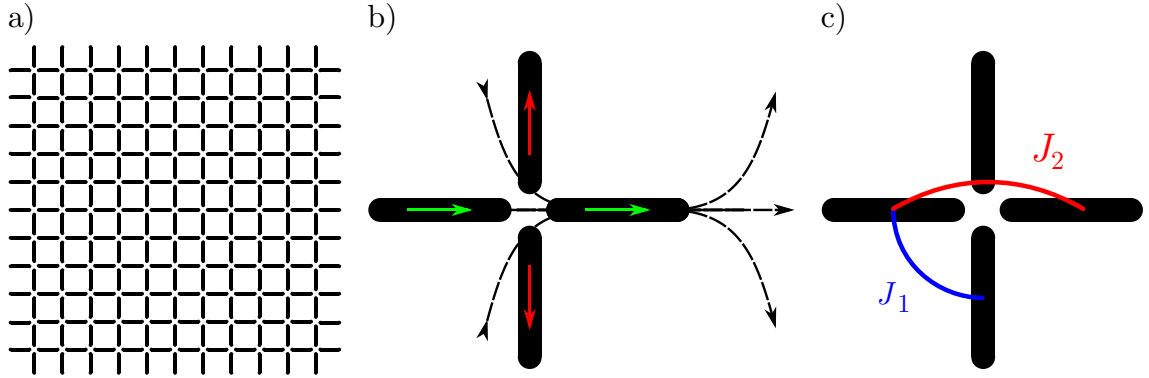
Fig. 2.2: a) The square lattice. b) The four magnets create a vertex where the orientation of other magnets is aligned with the leftmost nano-magnet but not with the rightmost nano-magnet. This creates frustration in the vertex. c) Interactions between first (J_1) and second (J_2) neighbours.

first and second neighbours, but always satisfy the "2in/2out" ice rule introduced by Bernal and Fowler [2].

2.3.1 Energy of the 16 vertex model

In this system, only the dipolar interactions between the first and the second nearest neighbours are considered. The Hamiltonian $\mathcal{H}$ describing such a system can be written as

$$\mathcal{H} = -\frac{1}{2} \sum_{\langle\langle ij \rangle\rangle} J_{ij} \sigma_i \sigma_j, \tag{2.1}$$

where J_{ij} is positive coupling strength for the first and the second nearest neighbour and σ_i and σ_j are scalars giving the spin's orientation along this direction. The expression $< ij >$ means that summation is made over the nearest neighbouring spins. Because $\sigma_i = \pm 1$ the spins can be considered as Ising variables.

Thanks to spin-reversal symmetry one can divide the 16 vertices into four groups. These groups (or types) are not characterised just by their symmetry but also thanks to their energy. When one considers interactions with just first and second neighbours the energies can be calculated by equations 2.2–2.5.

$$E_{\text{I}} = -4J_1 + 2J_2, \tag{2.2}$$
$$E_{\text{II}} = -2J_1 + 2J_1 - 2J_2 = -2J_2, \tag{2.3}$$
$$E_{\text{III}} = -2J_1 + 2J_1 - J_2 + J_2 = 0, \tag{2.4}$$
$$E_{\text{IV}} = +4J_1 + 2J_2, \tag{2.5}$$

where the J_1, resp. J_2, are coupling strengths of the first, resp. the second nearest neighbour. In this definition of vertex energies the coupling strengths are positive thus the $(-)$ sign corresponds to favourable and the $(+)$ sign corresponds to

unfavourable alignment. Another aspect of this energy level ordering can be seen when one assumes the first neighbour coupling strength is stronger than that of the second one ($J_1 > J_2$), thus the energies of corresponding types are higher for each type and the system tends to form type I vertices everywhere.

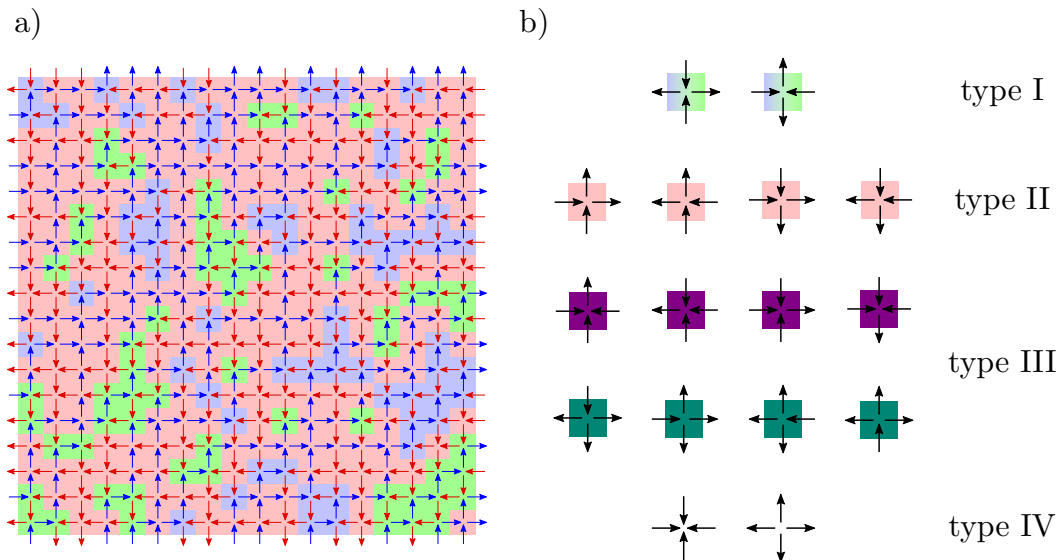### 2.3.2 Spin liquid phase in CSL

Fig. 2.3: a) Example of a typical spin-liquid state composed of a mixture of type I and type II vertices. In all spin configurations, the colour of spins (arrows) depends on the orientation by the next convention. Horizontal spins pointing to the right (resp. to the left) are blue (resp. red). Vertical spins pointing upward (resp. downward) are blue (resp. red). This convention helps to directly observe line ordering (typical example can be seen in figure 3.7b). Type I vertices are portrayed by light green and blue squares. Regions, where type I vertices are connected together, are then more recognisable. Type II which separates blue and green islands of type I is portrayed by light red squares. Spin configuration was obtained by Monte Carlo simulation. b) Overview of all 16 possible vertex configurations. Type I and type II are the only types that fulfil the so-called *ice rule*. Type III and type IV are excitations of the system and violate the ice rule. The spin configuration is adapted from [34].

The artificial spin liquid is a disordered but correlated magnetic state made by an assembly of interacting Ising variables and pairwise spin correlations that decay to zero at large distances [34]. Spin liquid phase or ice phase on a square lattice is a specific state that usually refers to a six vertex model in statistical mechanics that has an intriguing behaviour at zero temperature [22]. Because there are only six vertices out of the 16 possible variants which permit the so-called *ice rule* (two spins pointing in the vertex and two out of it) the model is then referred to as the six

vertex model (see figure 2.3) [29]. This means that only type I and type II vertices are considered thus yielding in an ice rule constraint [34].

When the coupling strengths of the first nearest neighbour J_1 and the second nearest neighbour J_2 are equal, the condition for reaching a spin-liquid regime is fulfilled. For this system, the ground state is formed by six possible vertex configurations with the same energy (See equation 2.2 and 2.3 for ice rule condition $J_1 = J_2$).

When the system is not in the ground state the other configurations - excitations will start to appear (see section 2.4.1). In such a manifold one can observe the exotic behaviour of the magnetic monopoles on the disordered background. By magnetic monopoles in spin ice one means classical quasi-particles carrying a magnetic charge and interacting via a Coulomb potential at long distances [9]. Determining the magnetic charge of a vertex is simple, one needs to add up all spins (arrows) pointing in a vertex and subtract all spins pointing out of the vertex. Each spin has a charge value equal to one. Because types I and II do not carry a magnetic charge the first excited vertex is type III ($q = \pm2$). A magnetic monopole with even higher energy is one with type IV ($q = \pm4$) but these excitations are energetically so unsuitable to be observed in such a manifold.

2.4 Coulomb phase

Coulomb phase physics was introduced by Henley in 2010 [16] to describe specific lattice models by using fundamental laws of electrostatics and magnetostatics. This concept is built on the idea of "lattice fluxes" and local vertex charges. Considering only lattice spin models Henley provides three conditions [16] for a Coulomb phase [34].

1. Each lattice variable (the spin in our case) can be mapped to a discrete signed (magnetic) flux $\mathbf{p}_i$, running along bond i.
2. At each lattice vertex, the sum of these signed fluxes is zero.
3. the system is in a highly disordered state (i.e., liquid-like).

Furthermore, Henley showed that the desired emergent vector field $\mathbf{P}(\mathbf{r})$ is the coarse-graining of these lattice fluxes and is divergence-free.

$$\nabla \cdot \mathbf{P}(\mathbf{r}) = 0. \tag{2.6}$$

The classical square lattice system and its liquid phase is a natural candidate for a Coulomb phase. Because of the ice rule condition, only type I and II are present and those types have zero magnetic charges thus condition 2 and corresponding equation 2.6 is fulfilled. Also, because the system is in spin liquid regime, it is degenerate too and condition 3 is fulfilled as well.

2.4.1 Magnetic monopoles in Coulomb phase

A question arises about how the system will behave when the equation 2.6 is locally disturbed by the presence of a defect (i.e. type III with non-zero magnetic charge). These defects are from the energetic point of view *excitations* of the spin liquid
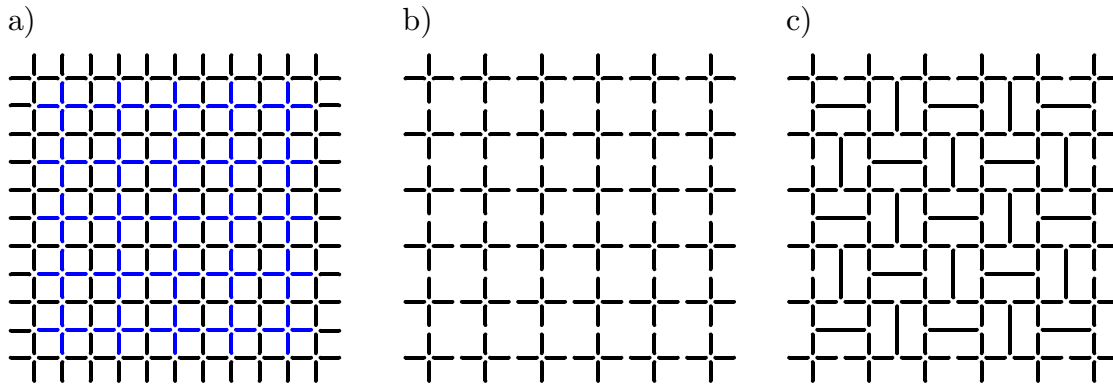
Fig. 2.4: a) Classical square lattice. In the first step, the blue magnets are removed. b) Big cross lattice. Empty spaces are filled with longer magnets in alternating horizontal or vertical directions. c) Long island shakti lattice.

manifold but mostly are referred to as magnetic monopoles. The reason why one would use the word monopole (and to top it all *magnetic* monopole) is the following. Excitations living on the highly disordered manifold have particle-like properties. In this sense, the background formed by type I and II vertices behaves like an uncharged vacuum in which charged particles repel and attract each other through Coulombic interactions. Observation of these dynamics and system phenomena on a lab-on-chip approach is currently a very interesting direction of scientific research [11, 10, 31].

2.4.2 Pinch points in reciprocal space

However, how to know that the spin system is in this Coulomb phase? Henley and others [16, 12, 38] showed that a Coulomb phase has specific diffraction features that leave fingerprints in reciprocal space. By Fourier transformation, one can obtain the magnetic structure factor (MSF) that carries important information about the system (see section 3.4.1). Due to a singularity in reciprocal space at certain values, one can observe a characteristic shape of a pinch point that unambiguously corresponds to a Coulomb phase.

2.5 Shakti lattice and mapping to the square ice

The classical square lattice was studied for decades and is still a very interesting geometry for the study of frustrated systems. But physicists in this field are still trying to invent new geometries with different properties [6, 36, 34, 26]. One of the rather new geometry is the shakti lattice [26, 37, 17]. This geometry is interesting in many ways. The first interesting thing is using two different vertex types with coordination numbers $z = 3$ and $z = 4$. Also one can see at first glance that not every nano-magnet is the same. In figure 2.4 one can see how the geometry of the shakti lattice is derived from the classical square lattice.

One can notice that with the coordination number $z = 3$ *new* type of vertices can be observed. This means that for the shakti lattice, the 16 possibilities of square lattice vertices are extended by another eight vertices. These new vertices can be divided into three categories. In figure 2.5 one can see all possibilities of configuration in the shakti lattice. For better clarity, we will name the 4 types of vertices with coordination number $z = 4$ as T_1, T_2, T_3 and T_4 and the 3 types of vertices with coordination number $z = 3$ as C_1, C_2 and C_3.
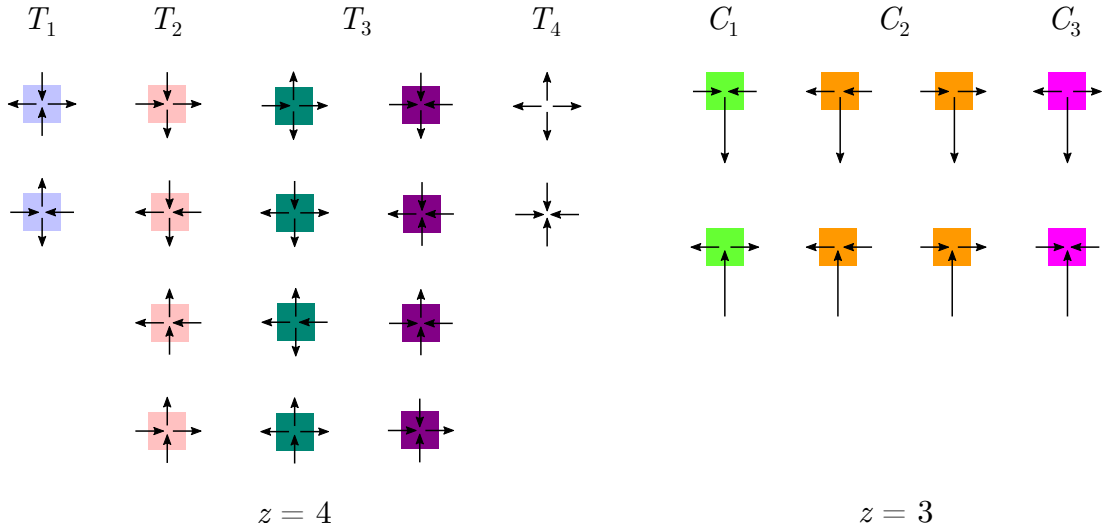
Fig. 2.5: All 16 possibilities of vertex configuration for a cross vertex ($z = 4$) and all 8 possibilities of vertex configuration for a T junction vertex ($z = 3$).

2.5.1   Shakti mapping

Fig. 2.6: Scheme of shakti lattice mapping to the square lattice by rules provided in [10]. Only black spins are part of the vertex plaquette and their orientation is important for the mapping. Green circles mark vertices with type C_2. The same circles are also visible in the circle notation. From the circle notation, one can assign the spin notation in the square lattice.

Chern et al. [10] describe a way how to transfer a more complex system (shakti) to a well-known one (square lattice). They also predict that this system can be mapped to a 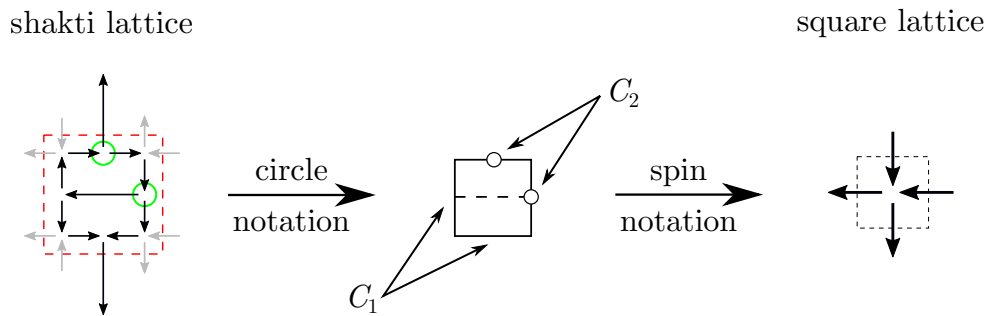six-vertex model if other conditions are fulfilled. And the most interesting prediction was that after mapping such a system we should obtain a spin-liquid phase in the square lattice.

To understand how the mapping works one needs to have a look at the vertices composed of type C. In our conditions where one should be close to the shakti ground state only types C_1 and C_2 are taken into account. In figure 2.6 one can see that in the square that contains the horizontal (or vertical) long magnet, are four vertices of type C. Because only two possibilities for the T-vertex are valid one can assign an arrow (or spin) pointing up or down for the top and bottom T-vertex and the same for the left and right T-vertex.
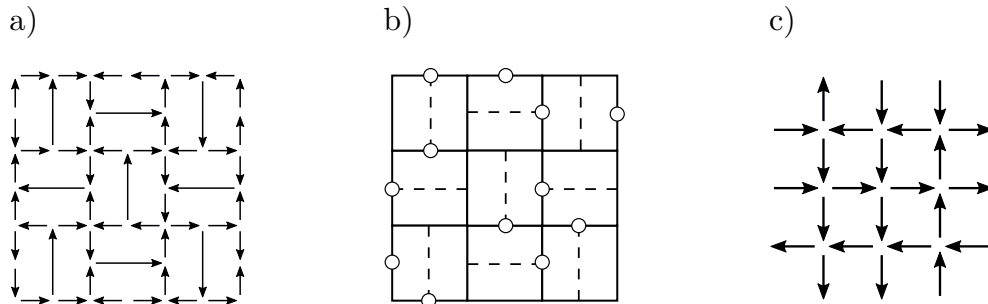

Fig. 2.7: a) Spin state in the shakti lattice with type T_1 at the cross vertices. b) Mapping to the circle notation by definition presented in figure 2.6. c) Emergent 6-vertex model after the mapping. Adapted from [10].

The definition of the mapping consists of only T_1 vertices at the cross vertices ($z = 4$) and only C_1 and C_2 at the T junction vertices ($z = 3$). This yields just two possibilities of configuration at the T junction vertices and because type T_1 is the only possibility for the cross vertices, one can have only six possible configurations on the shakti plaquette. These configurations can be defined as a vertex after the mapping (6-vertex model). A typical configuration can be seen in figure 2.7. This definition of mapping is useful only for experimentally unreachable conditions. Also, this model does not include excitations (i.e. monopoles) created by type III and type IV. For those reasons, an extension from the 6-vertex model to the 16-vertex model has been needed. In figure 2.8 all possible shakti configurations in the circle notation are present and their corresponding 16-vertex model configurations.
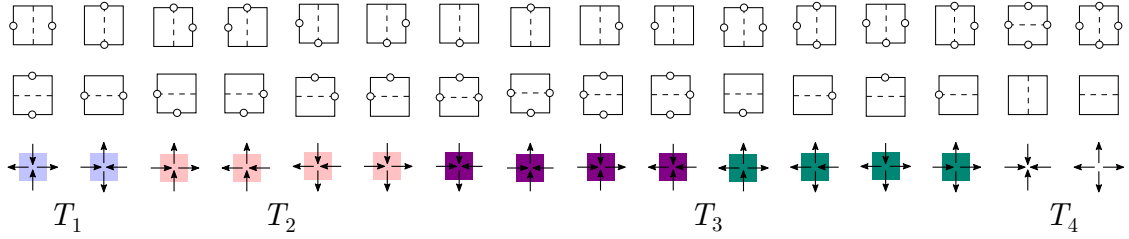
Fig. 2.8: Mapping between shakti geometry and square geometry. Dashed horizontal and vertical lines represent the direction of long islands. A circle between the corners of the square represents a T junction with vertex type C_2 and the same place without a circle represents a T junction with vertex type C_1.

2.5.2 Excitations in the new mapping model

This extension has one important impact on the shakti lattice system. To observe type III in the square system after the mapping, the rule of type T_1 only on the cross vertices must be broken. The excitation (type III) is linked with the mapping by having three times type C_1 (resp. type C_2) in its vertex. To achieve this state at least one of the four cross vertices must be formed by type T_2 or type T_3. Theoretically even by type T_4 but with our level of demagnetization protocol and its efficiency described in the section 3.2 the type T_4 has immense energy and it is, therefore, never observed.

To be more specific the condition for excitation creation is more complex. To better understand the situation let's label the four cross vertices as corners of the plaquette. From each of those four cross vertices, two spins (nano-magnets) are participating in the T junction vertices (spins with black colour) and two of them belong to the diagonal plaquette (spins with grey colour). These *corner spins* can generally have ferromagnetic ordering (FM) or antiferromagnetic ordering (AM). When the theoretical conditions are met one observes only type T_1 vertices at the cross vertices. In such a case corner spins are always ferromagnetically aligned. However, in experiments, this configuration is very challenging to obtain and the non-zero probability of other types than type T_1 at cross vertices is present.

Plaquettes with two C_1 and two C_2 types at the T-cross are types I and II after the mapping. For these two types, the general condition for the number of ferromagnetic and antiferromagnetic corner spins is as follows:

Rule 1 *The number of antiferromagnetic spin corners must be zero or an even number in a plaquette with two C_1 and two C_2 types.*

For plaquettes that project themselves to type III exists two main groups. These groups are defined by the number of C_1 (resp. C_2) types. Because type III in CSL lattice is referred to as a monopole at specific conditions described by Chern [10], these new type III groups will be named as C_1 (resp. C_2) monopoles depending on which number of C types is higher. Nevertheless, both groups must fulfil the FM or AM condition. In this case with three C_1 or C_2 types in the plaquette, at least one pair of corner spins must be aligned antiferromagnetically.

Rule 2 *The number of antiferromagnetic spin corners must be an odd number in a plaquette with three C_1 (resp. C_2) types and one C_2 (resp. C_1) type.*

Similar groups can be found for type IV vertices. Again, groups will be named C_1 (resp. C_2) type IV monopoles. Due to the even number of types C_1 or C_2 the number of antiferromagnetic corners spins must be even or zero.

Rule 3 *The number of antiferromagnetic spin corners must be zero or an even number in a plaquette with four C_1 (resp. C_2) types.*

These last two rules (2 and 3) have important implications. When one wants to observe interesting behaviour of excited defects (i.e. monopoles) on a disordered background formed of the spin liquid phase, types T_2 and type T_3 at the cross vertices must be present. With such an approach the disadvantage of achieving 100% population of T_1 at the cross vertices now becomes important and desirable property of the system.

3 Methodology

One of the great advantage of working with artificial spin systems is fabricating a large variety of desired lattices on a relatively small surface (e.g. 5000 lattices on 30 mm^2 area). This implies that when a sample is optimized one sample is more than enough. The sample used for this thesis was fabricated by Ing. Ondřej Brunn at the Institue of Scientific Instruments in Brno and further details will be provided in section 3.1.

To observe the exotic behaviour of artificial spin systems one has to bring them to their lowest possible energy. The methods to reach these low-energy states will be discussed in section 3.2 with emphasis on the method I used.

Once the sample is fabricated, magnetic force microscopy (MFM) imaging is used to determine the direction of magnetization of each nano-magnet in the lattice under examination. The basis of atomic force microscopy imaging will be discussed in section 3.3.

After measuring the magnetic response of the artificial system one needs to analyse the data. In section 3.4 the recognition process, the determination of the vertex populations before and after the mapping (see section 2.5.1), Monte Carlo simulations and other techniques used to post-process the data will be presented.

3.1 Fabrication of the sample
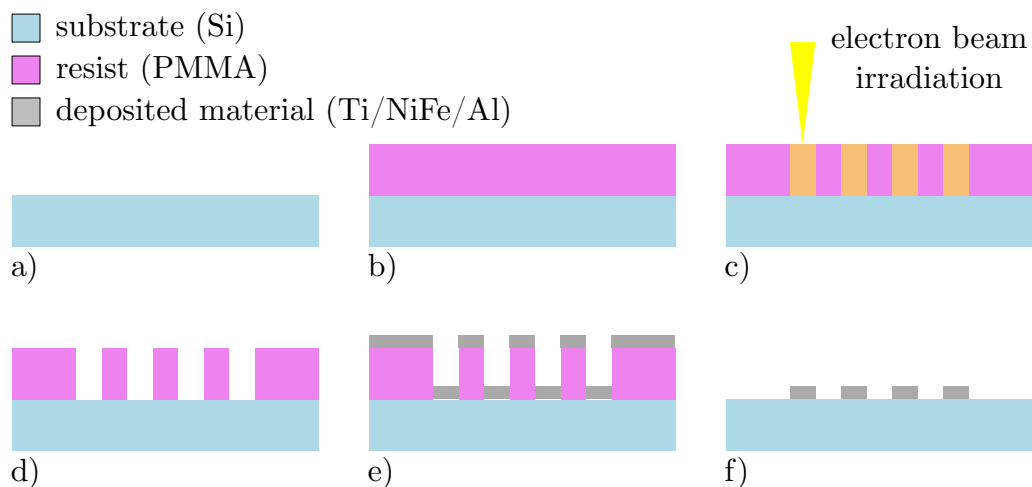
Fig. 3.1: Sample fabrication process: a) substrate preparation (e.g. Si), b) substrate is spin-coated with e-beam positive resist (e.g. PMMA), c) resist is exposed by electron beam lithography, d) resist is developed, e) desired material is deposited by vapour deposition, f) Unwanted material is lifted-off together with remaining resist. Adapted from [6].

For the sample, a silicon substrate with a native SiO$_2$ layer was used. The silicon substrate was spin-coated with a PMMA positive resist, which was irradiated with an electron beam at precise locations depending on the required parameters such as

the length and width of the nano-magnets and the geometry of the lattices. After electron beam exposure, the irradiated parts of the resist were dissolved by the developer. The metal layer is then evaporated and consists of an adhesive 5 nm layer of titanium a 25 nm thick layer of permalloy $Ni_{80}Fe_{20}$ and a capping layer of 3 nm thick layer of aluminium. The last step was to use a solvent to remove the resist with unwanted permalloy and aluminium. More details about the fabrication process can be found elsewhere [6, 36, 31, 28, 30].

3.1.1 Lattice parameters

In previous sections, the great advantage of artificial spin ice systems was already mentioned. The tunability of these systems is crucial and relatively easy thanks to the fabrication process described in section 3.1. One just needs to design a series of lattices (e.g. shakti lattices) with one or more varying parameters.

The main property of the lattice is the lattice geometry. Different geometries have obviously different parameters that can be tuned. Shakti geometry is derived from the classical square lattice as illustrated in figure 2.4, therefore describing the shakti parameters will be sufficient to understand the CSL parameters as well.

Designing the layout starts with the parameters of a single nano-magnet normally used in CSL. The parameters of this magnet are its shape, length, width and thickness. All lattices measured for this diploma thesis have an aspect ratio length divided by width defined equal to five. For better interactions, all nano-magnets (including long islands in the shakti lattice) have their ends rounded. The length of the nano-magnet already includes the rounding as can be seen in figure 3.2. The thickness of all nano-magnets is the same and depends on the fabrication process (see section 3.1). The last important parameter is the distance between nano-magnets. This distance is called the gap and its value is the same for nano-magnets interacting in a cross and at T junction. Sometimes different notations are used and a parameter called lattice spacing can be introduced [14]. For a full description of the shakti lattice, one just needs two parameters: the gap and the length of the nano-magnet. The rest (e.g. length of the long island) can be easily computed from the geometry presented in figure 3.2.
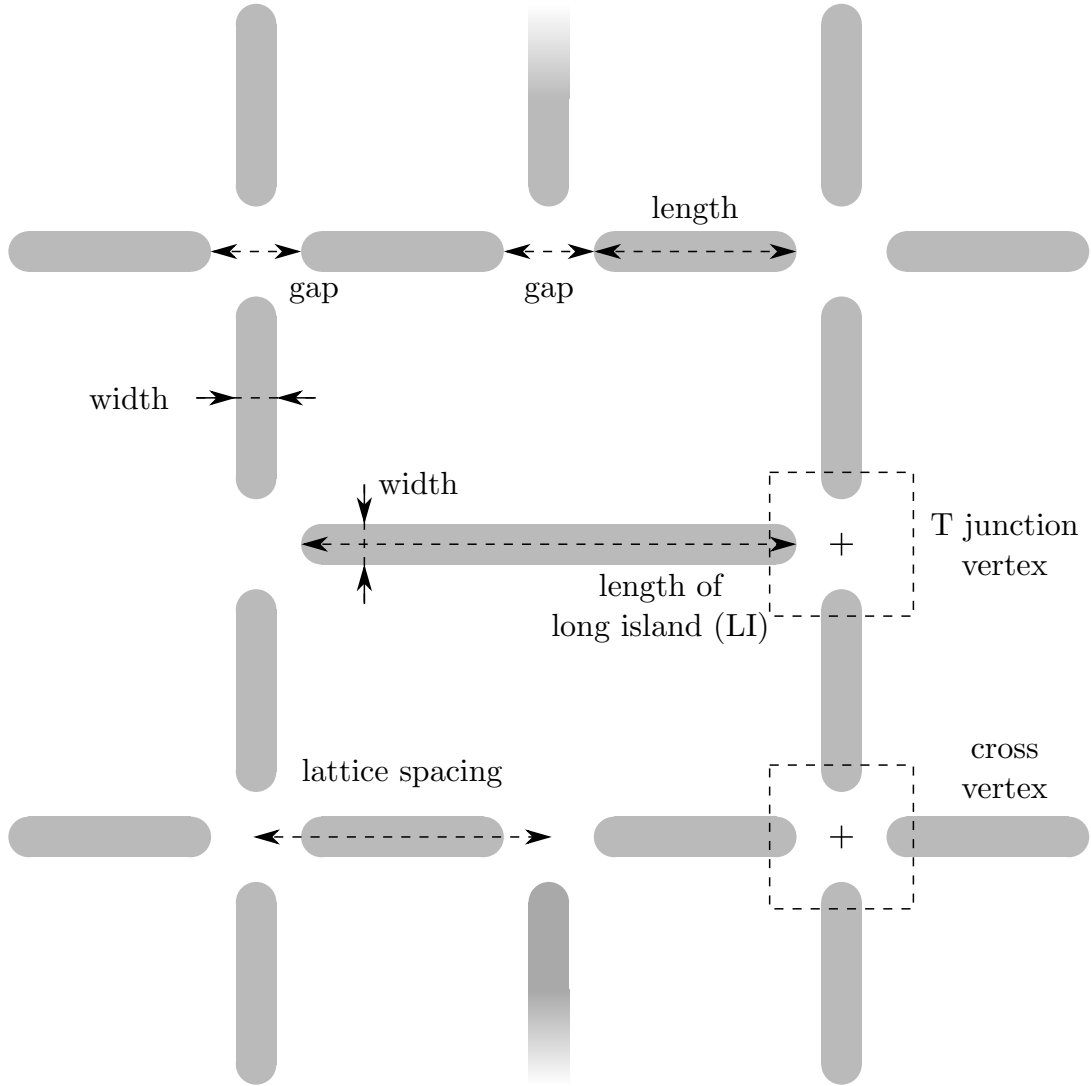
Fig. 3.2: Schematic description of the shakti lattice parameters. The gap between short and long nano-magnets is the same everywhere. The distance between the T junction vertex and the end of the long island nano-magnet is half of the gap distance. Lattice spacing is therefore equal to the length of a nano-magnet plus the gap, or to half of the length of the long island plus the gap. The cross vertex and the T junction vertex are marked with their centres.

3.2 Demagnetisation protocol

For estimating the quality of the field demagnetisation protocols, CSL lattices were used as a reference. As was mentioned in section 2.3.1, the ground state (i.e. a system with an effective temperature equal to zero) is an ordered phase containing only type I vertices [35].

Magnetization of these nano-magnets is randomly orientated after the manufacture. The interesting physics of frustrated systems appears when the effective

temperature is as low as possible. One needs to bring the artificial system to low energies and provide the system with the possibility to behave according to its neighbour's interactions.

There are several methods how to help the system to decrease its energy. The two mostly used approaches are the thermal annealing protocol [14, 40, 25, 32] and the field demagnetization protocol [39, 7, 8, 34]. In my case, the field demagnetisation protocol was used and will be more specified. In this approach, one can use an external periodical magnetic field that is decreasing in time (see figure 3.3b). A sample with fabricated lattices is placed on a sample holder which rotates between the poles of an electromagnet (see figure 3.3a). In the beginning, all magnets are polarised with the external magnetic field. But because the sample holder is rotating with greater frequency than the frequency of the magnetic field, the magnetization of nano-magnets is changing rapidly.

At some point, several nano-magnets stop changing their direction of magnetization, and because the external field has no longer the sufficient strength to flip a nano-magnet, magnetization freezes. The frozen nano-magnet then starts to affect its still-changing neighbours. At the end of this demagnetization protocol, one hopes that the system had relaxed for a sufficient time and that the system has found a low energy configuration.
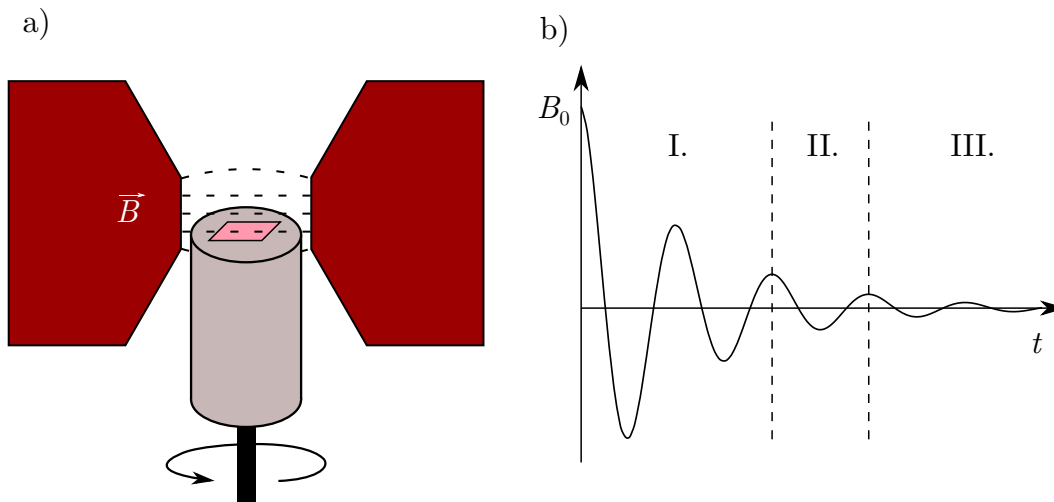

Fig. 3.3: a) Scheme of the demagnetization setup. The sample is placed on the rotating sample holder and between the electromagnet poles. b) Plot of a slowly decaying external magnetic field. During phase I, the external magnetic field is relatively strong and all nano-magnets follow the field direction. After some time (depending on the demagnetisation protocol) the magnetic field starts to be of the same order of magnitude as the critical field required for the spin-flip. This effective zone window is described by phase II in the plot. At the end of the second phase, some nano-magnets start to freeze and this effect is increased by additional field lowering. In phase III, the nano-magnets have found their best configuration for this procedure and the external field does not have enough strength to change magnetisation anymore.

3.3 Magnetic force microscopy

After a demagnetization protocol, one microstate of the 2^N (where N is a total number of spins e.g. 3000) possible configurations of the system is obtained. By using magnetic force microscopy (MFM) and by scanning the whole lattice one can read the orientations of all spins (e.g. magnetization) and have access to the magnetic microstate.

Magnetic force microscopy [23] is a scanning microscopy technique that is based on atomic force microscopy first introduced by Binning [3]. This method uses force interactions between a sharp tip and the sample of interest. If one uses specially treated tips such as tips with a magnetic coating, a magnetic image can be obtained. To separate the information about the topography of a sample and its magnetic behaviour, a two pass method is used. The sharp tip is oscillating near its resonant frequency (tapping mode) and probes topological information during its first pass. Then the tip is lifted up by a specified distance (mostly between 40 and 80 nm depending on the tip, sample and other circumstances). The second pass is conducted but now the tip mimics the topography with a constant distance (e.g. 80 nm). The contribution of attractive or repulsive force induced by the interaction between the tip and the surface of a sample is substantially reduced and only the interaction between the magnetic layer of the tip and the magnetic stray field coming out of the sample (a nano-magnet this case) is recorded.

When the stray field from the nano-magnet is parallel with the magnetization of the MFM tip, the repulsive or attractive forces are the largest. This force bends the cantilever of the MFM tip which then changes the path of the laser beam used to capture these small tilting movements (see the schematic description in figure 3.4). The result of the measurement is a scanned region with dark and bright circles depending on the orientation of the stray field coming *in* or *out* of the nano-magnet.
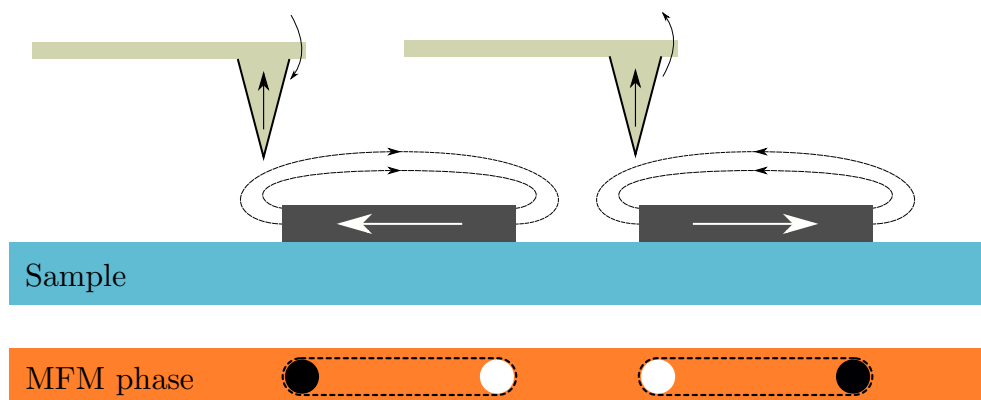

Fig. 3.4: MFM phase contrast and bending of the cantilever when probing the stray field. The result of the MFM measurement is a series of dark and bright dots depending on the orientation of the magnetisation of each nano-magnet.

3.4 Analysis of measured data

After basic adjustments in Gwyddion software, [27] (contrast modification, row alignment, smoothing) picture with magnetic phase contrast is uploaded into the evaluation MATLAB script provided by Ing. Ondřej Brunn. The first step is to select the lattice borders. The program then computes a mesh containing in each cell picture of one vertex (cross or T junction). During the first phase of evaluation, the cross vertices are examined (see figure 3.4b). One then has to distinguish among all 16 vertex configurations and select the right one by pressing the associated keyboard key. This process is repeated until all cross vertices are recognized. The second phase focus on T junctions and long nano-magnets. In this case, one does not evaluate the exact T junction vertex type but directly assigns a spin orientation of the long nano-magnet.
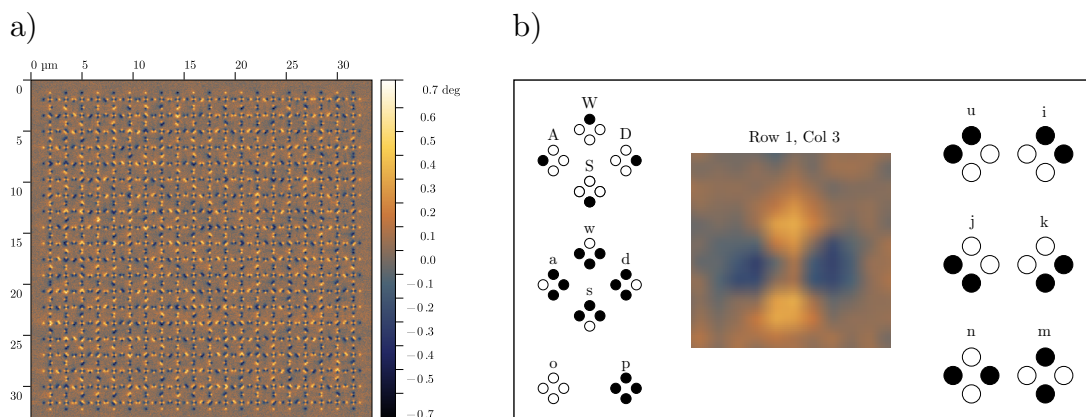
Fig. 3.5: a) A typical phase image from MFM measurement. After a preparation process, this figure is used in the evaluation script. b) The user interface of the evaluation script. In the middle of the screen can be seen a cropped region of the MFM image shown in a). The user has to press the corresponding key on a keyboard depending on the vertex configuration. On the left and the right side, all 16 vertex possibilities are shown with their corresponding keys. In this case, the user should press the button "n". Information is stored and the following vertex appears. This process continues until all vertices are evaluated.

After completing this process, several outputs are obtained. The first output is unsurprisingly a datasheet containing the spin configuration of the examined lattice in form of numbers associated with the vertex types. Thanks to this configuration, all other calculations and statistic properties can be made automatically.

The second important quantity describing a system is the vertex population. The evaluation script counts all vertices according to their types (T_1, T_2, T_3, T_4, C_1, C_2 and C_3) and provides their representation in percentages. Vertex populations are good indicators of the system's behaviour. They provide local information but not the system's correlations. However, they are very useful when some lattice parameter is changing (e.g. a gap between nano-magnets, their width, aspect ratio etc.), thus influencing the behaviour of the entire system.

Because a spin configuration in the form of dark and light dots scattered on the blurred background provided by MFM image is confusing for scientists in the field as well as for the wider public, a spin configuration in form of arrows was needed. Inspired by a code developed by Y. Perrin [30] for CSL lattices, an analogic vertex map for the shakti lattice has been developed (see figure 3.6a).

The last part of the script gives us a spin configuration of the shakti lattice after the mapping to the square lattice (see section 2.5.1). Because the system size is not infinite, the vertices at the boundaries are omitted. This reduces the system size but on the other hand, decreases the unwanted presence of the system's boundary. The definition of the mapping works only when there is type C_1 or C_2 at a T junction vertex. However, sometimes even type C_3 occurs and in such a case the associated spin is not taken into account and only an empty space is visible in the spin configuration. The spin configuration of both lattices (shakti lattice and CSL lattice after the mapping) are presented in figure 3.6.
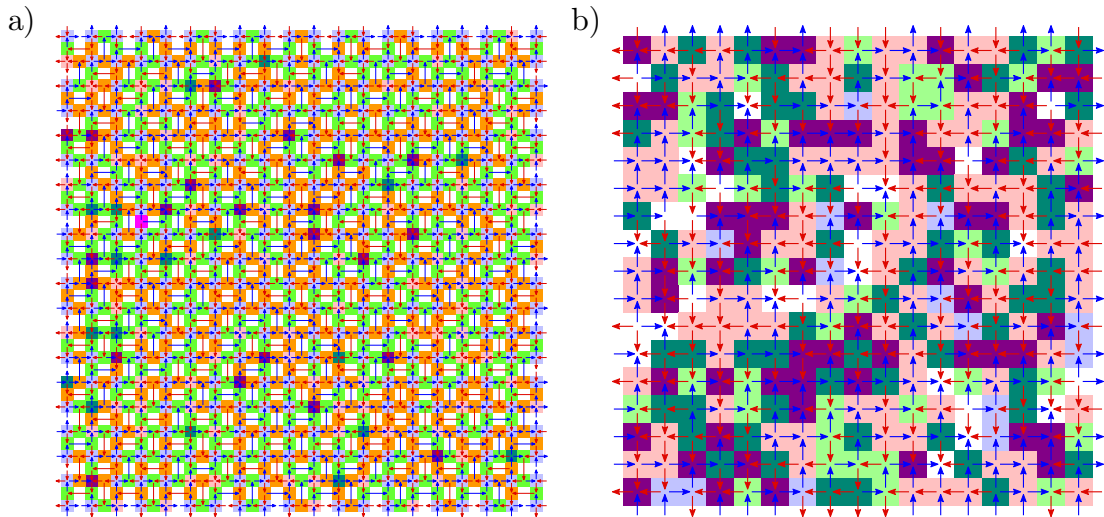

Fig. 3.6: a) The shakti lattice spin configuration is provided by the MATLAB script. The main significance of colours used in the shakti lattice configuration is the same as in the CSL described in figure 2.3 except the colour of T_1 vertex. In CSL two colours for type I are used: light blue and light green. This is not needed in the shakti configuration so only light blue colour is used for the T_1 vertices. Types of T junction vertices can be differentiated by green, orange and magenta colours corresponding to types C_1, C_2 and C_3, respectively. b) Spin configuration of CSL obtained after the mapping of the shakti lattice shown in a). Because the mapping (see section 2.5.1) and orientation of the spin in CSL is linked with the shakti lattice via the T junction vertices, one can see that one spin that corresponds to a type C_3 (magenta colour) in the shakti lattice is missing in the CSL lattice.

3.4.1 Magnetic structure factor

The magnetic structure factor (MSF) is a powerful tool for the characterisation of a spin configuration. A spin configuration obtained by MFM is represented in

reciprocal space by a Fourier transformation of pairwise spin correlations. The result of this computation is a diffraction pattern similar to one that can be obtained by a neutron diffraction experiment [34]. Computation of MSF is part of Y. Perrin toolkit developed during his Ph.D. thesis where additional details concerning this technique can be found.[30].

When the system is ordered, the MSF gives magnetic Bragg peaks at specific locations in reciprocal space. However, when the system is disordered (e.g. spin liquid phase) the MSF is diffuse and has a specific shape [33]. MSF then looks like a series of squares connected by their corners. Where two corners intersect, the so-called pinch-points are visible [16, 33] (see section 2.4.2).
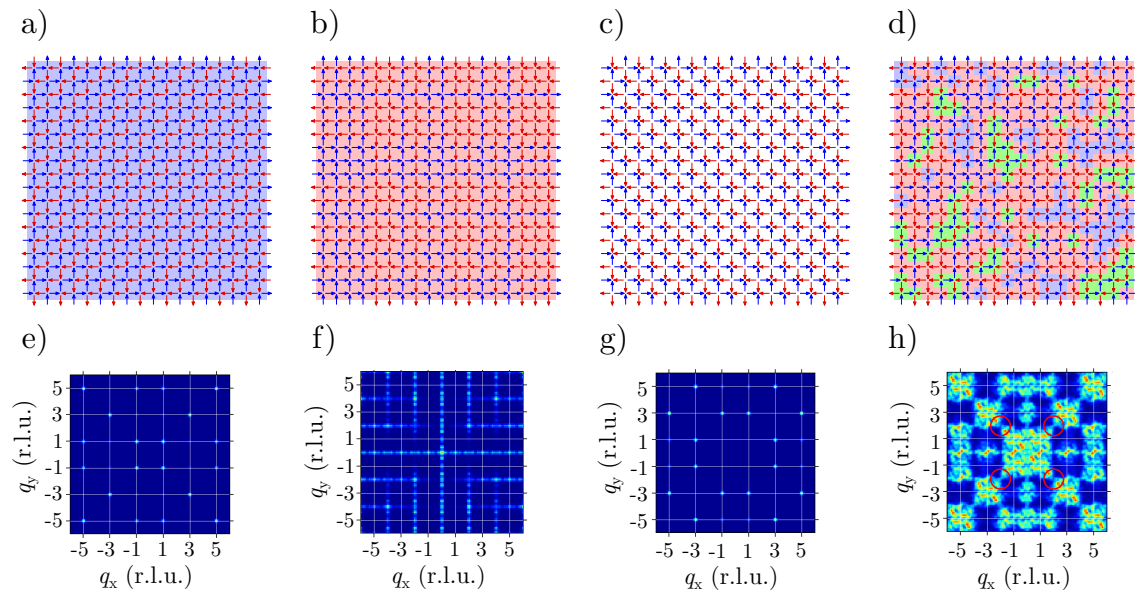

Fig. 3.7: Spin configurations and their corresponding MSF. a) tiling of type I vertices, b) spin configuration of random arranged fully polarized lines created by type II vertices, c) all-in/all-out ordered phase of type IV, d) spin liquid phase with a disordered mixture of type I (light green and light blue vertices) and type II (light red vertices). The spin configuration is adapted from [34]. In e)–h) magnetic structure factors are shown for lattices a)–d) respectively. For this overview, only type IV tiling in g) was chosen but one can expect some intensity at the very same q-vectors with type III tiling. The fingerprints of the spin liquid phase, the pinch-points, are highlighted by red circles in h).

3.4.2 Monte Carlo simulations

Monte Carlo simulations (developed by B. Canals at Institut Néel) are used for calculating MSF for a wide range of models and temperatures. However, these simulations do not provide just magnetic structure factors for desired temperatures, they also provide useful results, such as pairwise spin correlations, nearest neighbour charge correlators, entropy density and specific heat or population dependencies on the effective temperature. Simulations of the dependence of Monte Carlo population curves (MC curves) on temperature are essential for this thesis.

For the analysis of artificial spin systems, several approaches were mentioned (e.g. spin configuration, populations of vertices, MSF). The last approach that was used in this project was to determine the effective temperature of the system. To assign a temperature correctly one has to do two things. First is to use the right model i.e. fitting experimental data on a model that should describe an experiment. The second part is to place experimental data on the Monte Carlo curves with the smallest mismatch.
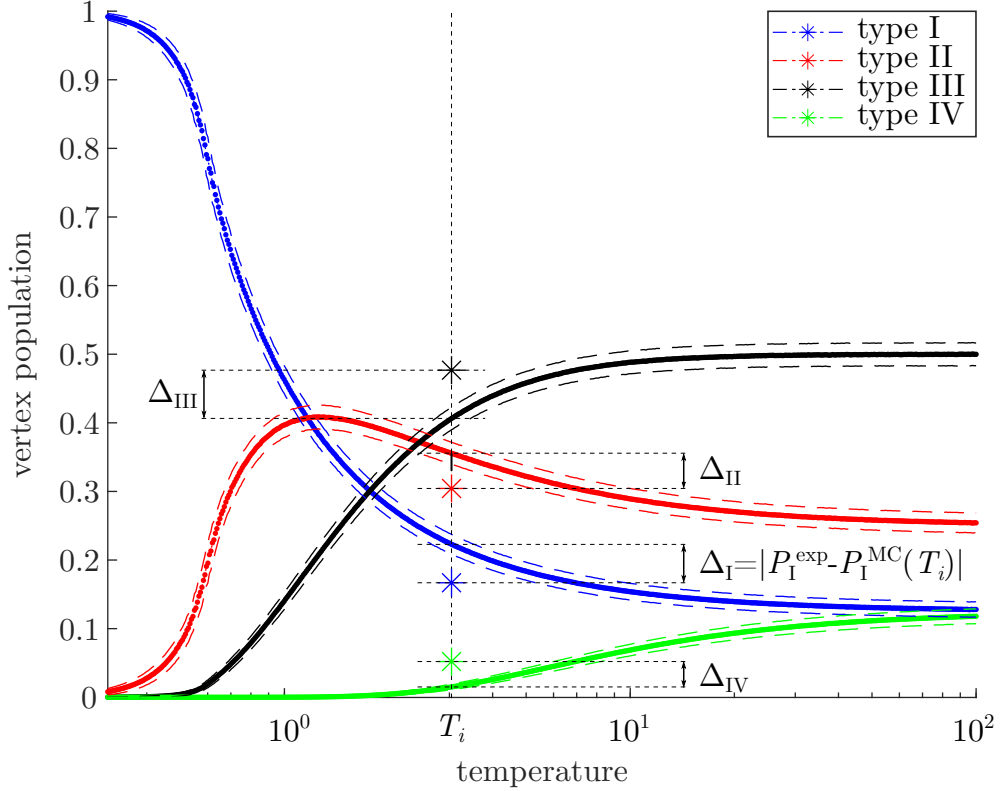

Fig. 3.8: Monte Carlo simulation of population curves for a model with only first and second neighbour interactions. Experimental values are depicted by star markers where each colour corresponds to the colour of MC curves. During the fitting process, the difference between the experimental and simulated populations is calculated for each temperature (difference Δ_j). The accuracy of the fit is then $\sum_{j=\mathrm{I}}^{\mathrm{IV}} \Delta_j^2$. The effective temperature for the selected model is the temperature with the value of the overall square difference closest to zero.

Using the correct model to describe the physics of the system is a complex task and these issues will be discussed in later chapters (see sections 4.3.1 and 4.3.2). Here, the more technical part of the fitting process should be addressed. After the evaluation process and mapping to the square lattice, one obtains four values corresponding to the population of each of the four vertex types ($P_{\mathrm{I}}^{\mathrm{exp}}$, $P_{\mathrm{II}}^{\mathrm{exp}}$, $P_{\mathrm{III}}^{\mathrm{exp}}$ and $P_{\mathrm{IV}}^{\mathrm{exp}}$). These four values are then compared with values simulated for a certain temperature T_{i} that is probing a temperature range given by the parameters of a simulation ($P_{\mathrm{I}}^{\mathrm{MC}}(T_i)$, $P_{\mathrm{II}}^{\mathrm{MC}}(T_i)$, $P_{\mathrm{III}}^{\mathrm{MC}}(T_i)$ and $P_{\mathrm{IV}}^{\mathrm{MC}}(T_i)$). This comparison is done

for each temperature (the exact number of steps depends on the accuracy of the simulation). In each step, the difference between the population obtained from an experiment and one from a Monte Carlo simulation is squared and summed over all types ($\sum_{j=\mathrm{I}}^{\mathrm{IV}}[P_j^{\mathrm{exp}} - P_j^{\mathrm{MC}}(T_i)]^2$). This value then reflects the accuracy of the fit for a certain temperature T_i. The final effective temperature T_{eff} of a system is the temperature for which the value of the accuracy is the highest.

4 Results

4.1 Ice physics in the shakti lattice

To observe the ice phase in the shakti lattice, one needs to have $100\,\%$ vertex population of type T_1 at the cross vertices. Each lattice, defined by its gap, has three copies, which means that 30 lattices were measured. Each shakti lattice has 20×20 cross vertices which can be mapped to 19×19 vertices in CSL. Because of the finite size of the system, the mapped CSL borders are omitted, thus the final CSL has 17×17 vertices (see section 3.4). The population of the lattices with the same parameters was averaged and standard deviation was also added. Two regimes can be observed in figure 4.1a for vertex population of type T_1 and type T_2. For larger gaps, the vertex population of these two types is almost constant. However, when the gap is smaller, it is interesting to see a substantial decrease of type T_1 that is compensated by an increase of type T_2. This has an important impact on the formation of type III and type IV vertices after the mapping which disturbs the ideal spin liquid configuration. On the other hand vertex population of type T_3 is negligible for small gaps but with larger gaps, the interaction strength is decreasing, while the possibility of excitations (i.e. type T_3) in the system is growing. The vertex population of type T_4 is zero for all measurements. In figure 4.1b the vertex population for T junction vertices can be seen. For larger gaps, the population of type C_1 and type C_2 is balanced around $50\,\%$ but type C_1 is always more favoured than type C_2. For smaller gaps, the vertex population is unbalanced and the coupling strength favouring the formation of type C_1 vertices is winning. The vertex population of type C_3 is almost zero for all measurements. The field demagnetisation protocol was used (see section 3.2) for the 72-hour long procedure with the initial magnetic field $B_0 = 37$ mT. The quality of the demagnetisation protocol was confirmed by measuring the CSL lattices with 39×39 vertices (see figure 4.1c).
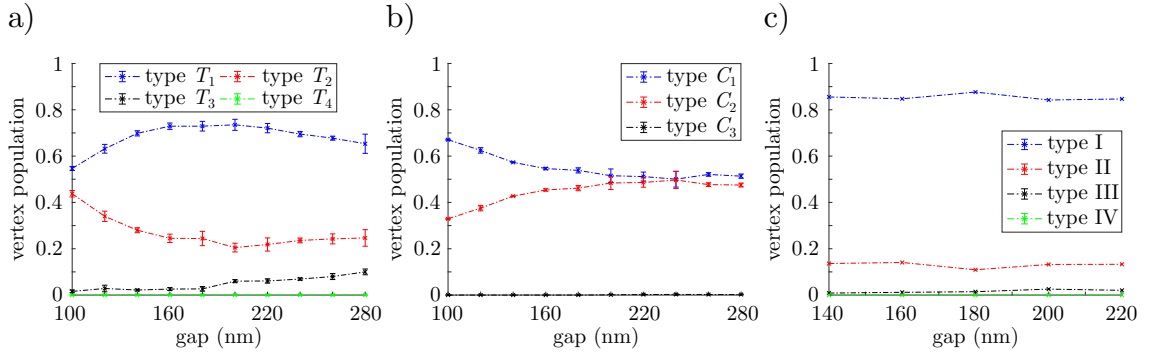
Fig. 4.1: a) Vertex population plot of cross vertices in the shakti lattice. Type T_1 which is crucial for the mapping to the spin liquid grows to a maximum value of about $75\,\%$ and then slowly decreases. b) Population plot of T junction vertices. Type C_1 is dominant for lattices with small gaps but the population difference between type C_1 and type C_2 decreases with larger gaps. c) Population plot for reference CSL lattices. Measurement was done only for CSL lattices whose gaps corresponded with the highest type T_1 representation in the shakti lattices.

In figure 4.2a can be seen the spin configuration of the shakti lattice and in figure 4.2b can be seen the spin configuration of the shakti lattice after the mapping for the 180 nm gap. The first striking difference between this spin configuration and the spin configuration of a spin liquid (see figure 2.3) is in a non-negligible amount of type III (32 %) and type IV (7 %) which should not be present in pure spin ice. One could imagine that the reason for the presence of type III and type IV in the CSL lattice is that they are excitations of the system and behave like magnetic monopoles scattered on the spin liquid background of type I and II as was described in section 2.4.1. Another argument supporting this hypothesis is the population of type T_1 in the shakti lattice (which is about 75 %) that enables the creation of excitations after the mapping (type III and type IV). Two crucial arguments will be presented to explain why the system after the mapping is not in the spin liquid phase.
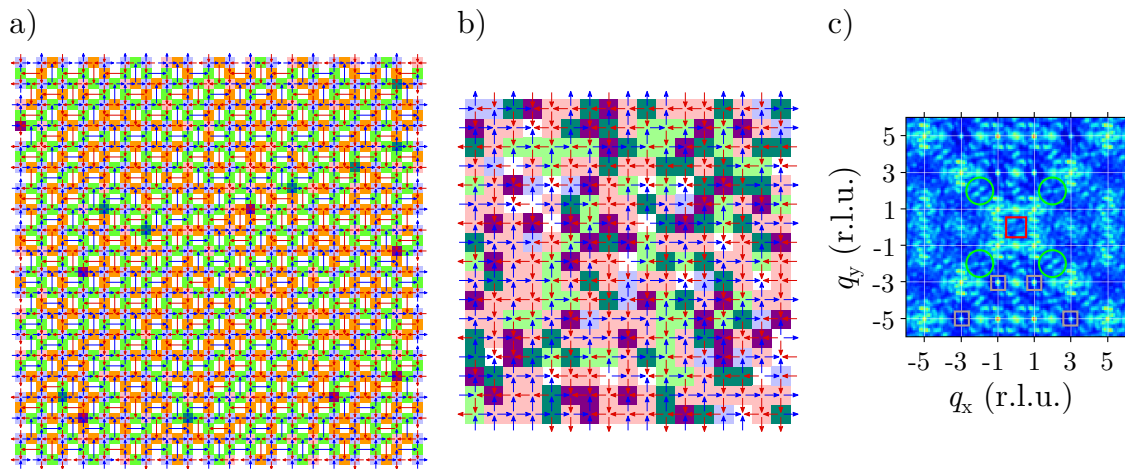
a)   b)   c)

Fig. 4.2: a) Spin configuration of the shakti lattice with 180 nm gap. Colours used for the vertices are the same as in figure 3.6a b) Spin configuration of the shakti lattice after the mapping for the shakti lattice presented in a). The presence of charge alternating clusters of type III with positive magnetic charge $q = +2$ (violet vertices) and negative magnetic charge $q = -2$ (dark green vertices) is visible. c) Corresponding MSF for spin configuration in b). Several proofs of the spin liquid absence are present such as missing pinch points (green circles), a considerable drop of intensity in the middle (red square) and the presence of emergent Bragg peaks at the positions associated with all-in/all-out vertices (grey squares).

Another indicator for the ice phase observation in the shakti lattice should be the equilibration of type C_1 and type C_2 at the T junction (see figure 4.1b). This can be observed for lattices with a 200 nm gap and larger. The population of type C_3, which does not allow the mapping (see section 2.5.1), is very low for all measurements and the mapping is not possible only for a negligible amount of vertices. However, the population of individual types is not sufficient enough to fully characterize the system because it does not carry information about the correlations.

The first interesting thing is the behaviour of "monopoles" which are clustering together and forming chessboard islands thanks to their magnetic charge alternation (dark green and violet vertices). In the Coulomb phase, monopoles can freely move

through the disordered background and behave like electrostatically charged quasi-particles. In this case (see figure 4.2b) "monopoles" tends to be together but they do not annihilate and rather form the chessboard clusters. The movement of these clusters through the background is not possible without increasing the energy of the system. From this, one can conclude that excitations are not Coulomb-like and could not be named monopoles.

The second question then arises what exactly is the background made of? Just by looking at the spin configuration, one would be tempted to say that there is a disordered mixture of type I and type II and that type II has more representation than type I, thus some assumptions are met for the spin liquid phase. For this characterisation can be used more precise technique which also includes the magnetic correlations of the system that are important ingredients in the spin liquid phase. The magnetic structure factor (MSF) carries all of this information as was mentioned in the section 3.4.1.

By a simple comparison of figure 4.2c and 3.7h, several differences can be directly seen. The most important difference is the absence of pinch points typical for the Coulomb phase and the spin liquid marked by green circles in figure 4.2c. Also, the typical squares are not visible but rather separated islands are present and the connection by "bridges" in the form of the pinch points is missing. Another proof of the absence of the spin liquid phase is the considerable drop of intensity in the centre of the MSF ($q_x = 0$ and $q_y = 0$). If one takes a closer look at the emergent Bragg peaks marked with grey squares in figure 4.2c, their position is the same as for the expected intensity of type III and type IV tiling (see figure 3.4.1g). On the other hand, in the MSF of pure spin liquid (see figure 3.4.1h) these Bragg peaks are not present due to the absence of type III or type IV.

The same results can be seen for other lattices. None of them exhibited the typical MSF of spin liquid and charge crystallisation for type III vertices was still present. An explanation is offered that the reason for the observation of this unexpected physics in artificial spin systems is that the effective temperature of these systems is not sufficiently low to be able to exhibit the ice phase as predicted in [10]. Further increase of type T_1 vertices in the shakti lattices is difficult due to the limitation of field demagnetisation. The quality of the field demagnetisation protocol was not assessed only by the population of type T_1 in the shakti lattice but also in reference CSL lattices. The vertex population plot for the CSL lattice can be seen in figure 4.1c.

However, Gilbert et al. used a thermal annealing procedure to lower the effective temperature of the system and managed to get a substantially larger number of type T_1 at the cross vertices [14]. It is appropriate to reanalyze their results with the methodology presented in this thesis and hopefully see the anticipated liquid phase.

4.2 Reanalysis of the literature

Gilbert et al. provided the MFM image of their measurement of the shakti lattice with the highest number of type T_1 vertices (around 80 %) [14]. The corresponding reference CSL lattice had a type I population of around 95 % which indicates the very good quality of the thermal procedure. The parameters of their shakti lattice

were slightly different from the lattice parameters used in my experiments. They used nano-magnets with a height of 25 nm, a length of 220 nm, and a width of 80 nm. The lattice spacing for their best lattice was 320 nm, thus the gap between two nano-magnets was 100 nm (see figure 3.2 with the lattice parameters).

However, only the MFM image and the population of the shakti lattice were presented. The mapping to the CSL was done only for tightly cropped region with only 4x4 vertices after the mapping. Even with the population of type T_1 around 80 % there was still around 20 % of type T_2 which brings excitations to the system as was explained in the section 2.5.2. With the extended definition of the shakti mapping the whole lattice can be used even with type T_2 vertices. In figure 4.3 can be seen the spin configuration of the shakti lattice obtained from [14] and its corresponding spin configuration after the mapping and the MSF of the mapped lattice.
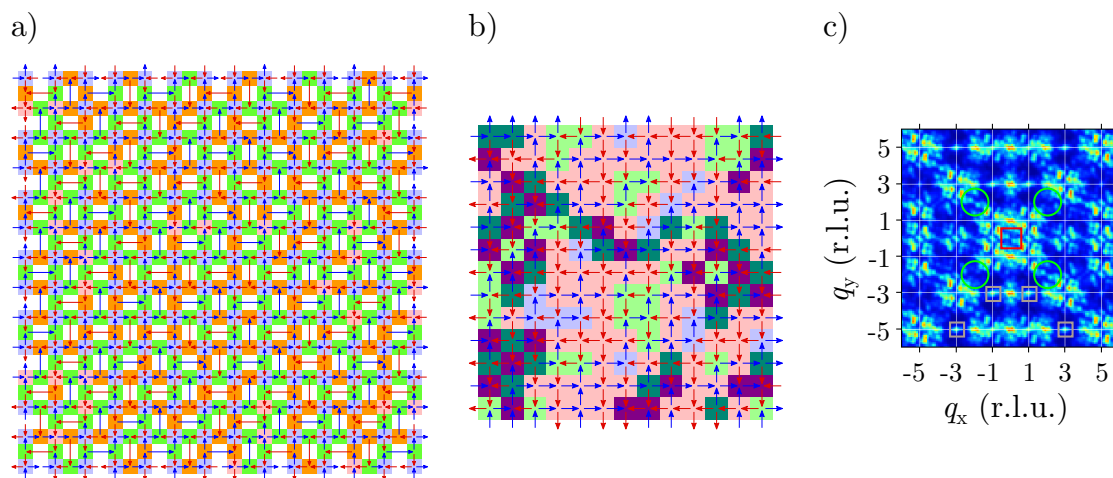
a)   b)   c)

Fig. 4.3: a) Spin configuration of the shakti lattice from [14]. For the mapping were also used the border vertices because the MFM image is only a cropped part from a larger system. This will substantially increase the statistics for further analysis. b) Spin configuration of the shakti lattice after the mapping for the shakti lattice presented in a). One can see a mixture of type I and type II vertices and a large amount of type III vertices in clusters with alternating charges (dark green and violet vertices). c) MSF for the spin configuration in b). The very same results as in 4.2c can be seen. Missing pinch points (green circles), a significant drop of intensity in the centre (red square) and the presence of ordered type III vertices (grey squares).

These results are again surprising. Even in a system with slightly different parameters (different widths and lengths of the nano-magnets), one can observe the same non-liquid-like behaviour of the system. The first thing that one can see clearly is the large number of type III vertices and they, again, form clusters with alternating charges (see figure 4.3b). The background looks like a disordered mixture of type I and type II vertices, but the analysis in reciprocal space provided by MSF (see figure 4.3c) exhibits the very same behaviour as in my results (see figure 4.2c). The absence of the pinch points (green circles) and intensity drop in the centre of the MSF ($q_x = 0$ and $q_y = 0$) marked by red square proves that the right model

that describes the physics observed in these systems is not the square ice model. Reaching the predicted spin liquid phase is even more difficult than what was expected even for shakti lattice with 85% of type T_1 (The cropped MFM image has even better population of type T_1 than the whole lattice presented in population plots in [14]).

4.3   Analysis of my measurements

It is suitable to check that the square ice model is not the right model for the whole set of my measurements. For this confirmation, Monte Carlo simulations can be used. The square ice model must fulfil such a condition where coupling strengths of the first nearest neighbour J_1 and the second nearest neighbour J_2 are equal (see section 2.3.2). The populations of vertex types should fit on the population curves computed for the condition $J_1 = J_2$ and the Hamiltonian $\mathcal{H}$ defined by equation 2.1. In figure 4.4a can be seen results of the fitting for all 30 lattices (thin star markers) and the lattice provided by Gilbert (thick star markers). It can be seen that most of the results do not fit well the MC curves, except for the Gilbert data points and some of my measurements.
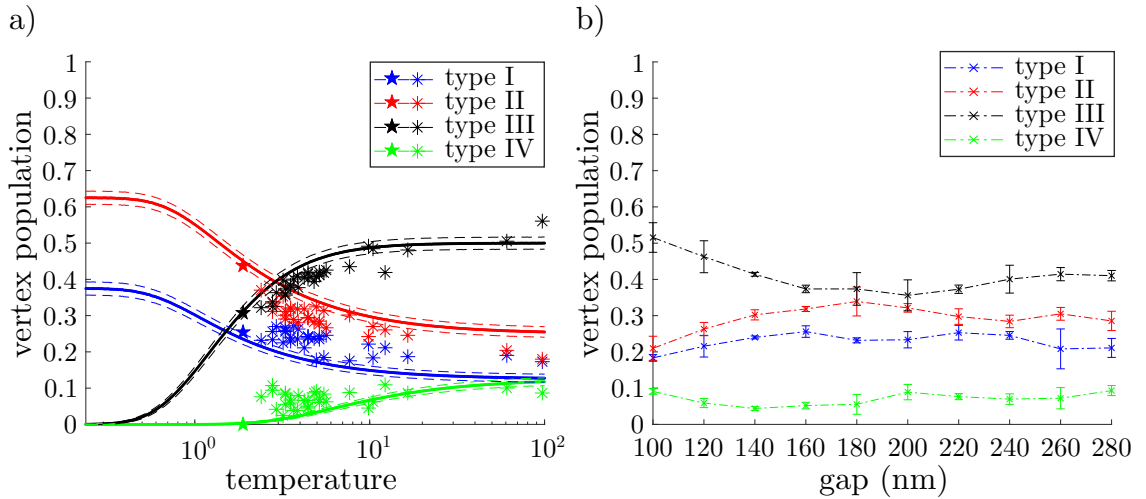

Fig. 4.4: a) Monte Carlo simulation for vertex populations depends on the system's temperature. Dashed lines are standard deviations provided by the simulation for each population curve. The lowest effective temperature is for the Gilbert lattice (thick star markers) but is still too high to reach the spin liquid phase at the lowest temperature. Thin star markers label my measurements. All data sets are moved to the higher effective temperatures which corresponds to a slightly worse quality of demagnetisation. b) Population plot of the shakti lattices after the mapping. For each gap, three lattices were measured and the averaged populations are presented with standard deviation bars. One can see a sharp decline for the type III population and a slow increase for larger gaps. An opposite behaviour can be seen for type I and type II. Type III and type IV play a significant role in the system for the whole variety of gaps.

Because of the mapping, the differences between type III and type IV are not as large as in conventional CSL. The presence of type IV is natural for the system in the same manner as the presence of type III. Furthermore, type IV vertices also tend to cluster together, thus their charges alternate as well as type III vertices. The energies of vertices are more complex than described in section 2.3.1 so one can afford to merge the populations of type III and type IV vertices and take them as collective excitations of the system (see section 4.4 for further explanation of the energies).

To find a better model that would describe the system one needs to change the shape of the type I and type II curves. In figure 4.4a almost all population results for type I and type II are between the MC curves for type I and type II. Because one is not bound with the $J_1 = J_2$ condition anymore, a simple change of the J_2/J_1 ratio will tune the shape of MC curves.

Also, from the population curve after the mapping (see figure 4.4b) several implications can be made. The lattices with very small gaps (i.e. 100 nm and 120 nm gaps) have a significant number of type III (and type IV) vertices. In the middle of the population curve for lattices with gap around 180 nm one can see the highest population of type I and a significant drop of the type III population. For larger gaps, the population curves are rather flat. This simply implies that observation of a different behaviour for these groups is probable.

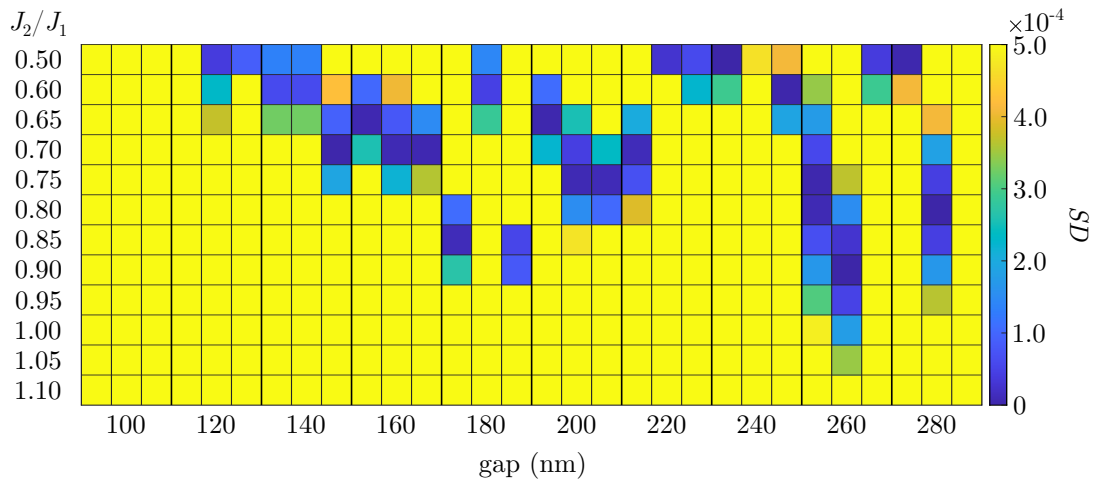### 4.3.1 MC simulations with a different J_2/J_1 ratio

Fig. 4.5: Results of the Monte Carlo simulations for different J_2/J_1 ratios. Each column indicates one lattice (i.e. 30 lattices). For each gap parameter and lattice copy (a, b and c) a label is placed. Each row represents the simulations with the corresponding J_2/J_1 parameter (i.e. 12 simulations). The colour scale is set by the threshold value of the square difference parameter $SD_{\max}$ that was set to $5 \cdot 10^{-4}$. Cells with a deep blue colour are fitted with the highest accuracy. Cells with yellow colour cannot be considered as good fits.

Monte Carlo simulations for population curves are a good point to start but they cannot determine the right model itself. For each lattice twelve different values of the J_2/J_1 ratio were used. The best fitting for each of these simulations was done by minimising the overall square difference as described in section 3.4.2. Ideally, the MC fitting would provide only one unique result for each lattice. However, for only slightly different J_2/J_1 ratios the population curves do not differ much thus the fitting is suitable for a wider variety of ratios. The following strategy was used to analyze these simulations. A threshold has been set by the value of the overall square difference. The simulations that passed this filter were plotted in a heatmap (see figure 4.5). Each cell in this heatmap represents the result of the fitting for the corresponding lattice and the fitting parameter. The threshold was set to $SD_{\max} = 5 \cdot 10^{-4}$. It was observed that this value is sufficient for good accuracy.

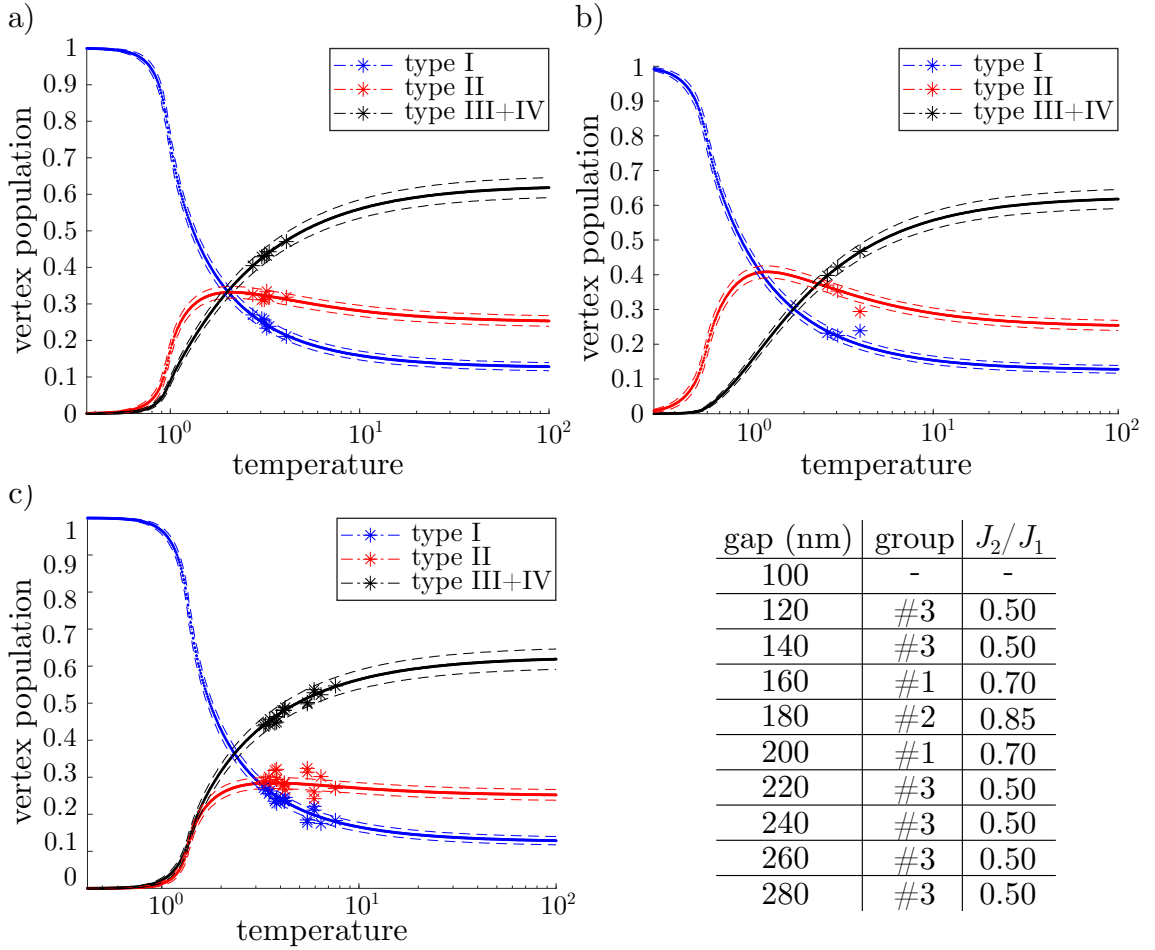| gap (nm)	group	J_2/J_1
100	-	-
120	#3	0.50
140	#3	0.50
160	#1	0.70
180	#2	0.85
200	#1	0.70
220	#3	0.50
240	#3	0.50
260	#3	0.50
280	#3	0.50

Fig. 4.6: Monte Carlo simulations fit for three groups depending on their gap and fit accuracy shown in figure 4.5. a) MC simulation for group #1 with $J_2/J_1 = 0.70$ and for 160 and 200 nm gaps. b) MC simulation for group #2 with $J_2/J_1 = 0.85$ and for 180 nm gap. c) MC simulation for group #3 with $J_2/J_1 = 0.50$ and for 120, 140, 220, 240, 260 and 280 nm gaps. Type III and type IV populations were merged for the reasons described above.

In figure 4.5 can be seen the formation of groups. Lattices with small gaps tend

to have a lower J_2/J_1 ratio (and for 100 nm gap probably and for larger gaps the ratio grows. Around the 180 nm gap (lattice with the best match with Gilbert measurement and closest to the predicted liquid phase) the best fit has a ratio around $J_2/J_1 = 0.85$ and for larger gaps ratio decreases. For very large gaps a different behaviour can be seen and several ratios can be used with high accuracy of the fitting. One can compare these "groups" with those obtained by analysing the vertex population curves for the lattice after the mapping (see figure 4.4b) and see a direct connection. To investigate this "package method" the measured results were divided into three groups depending on the fit accuracy.

The results in figure 4.6 clearly fit more accurately than the model with $J_1 = J_2$ shown in figure 4.4a. Also, by tuning the gap parameter in the shakti lattice one does not affect only the effective temperature of the system after the mapping but also the key parameter of the model itself, i.e. the J_2/J_1 ratio. These results suggest that a model describing shakti physics was found. However, the right model must provide the vertex population agreement and the magnetic correlations. For that, the agreement between MSF provided by Monte Carlo simulations and MSF from measurements is needed.

In previous sections was shown that type III and type IV vertices are more represented than expected but also they cluster together and form the chessboard pattern with their alternating magnetic charge (see the spin configuration in figure 4.2b and 4.3b). This magnetic correlation is not encoded in the MC population curves but emerges in the MSF at specified locations in reciprocal space as Bragg peaks (see grey squares in figure 4.2c and 4.3c). However, this tiling of type III and type IV vertices is not favoured in the Hamiltonian used for the simulations. Another ingredient must then be added to support the clustering of type III and type IV.

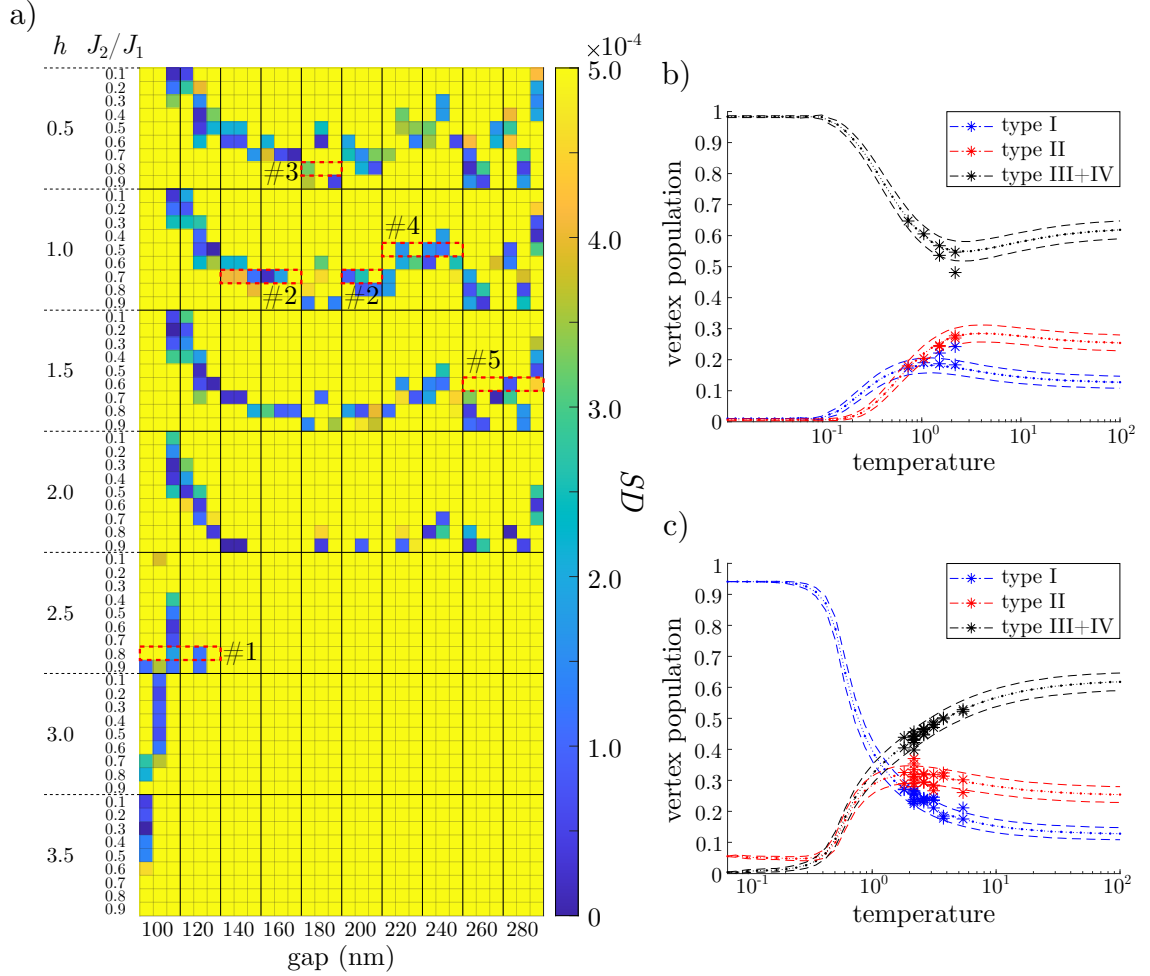## 4.3.2 MC simulations with a local magnetic field h

Fig. 4.7: a) Results of the Monte Carlo simulations for different J_2/J_1 ratios and several h values. Each column indicates one lattice. For each gap parameter and lattice copy (a, b and c) a label is placed. Each row represents the simulations with the corresponding J_2/J_1 and h parameters. The colour scale is set by the threshold value of the square difference parameter SD_{max} that was set to $5 \cdot 10^{-4}$ same as in figure 4.5. The division into five groups used in figure 4.9 is depicted by red rectangles. The h value orders cells. Cells with a deep blue colour are fitted with the highest accuracy. Cells with yellow colour can not be considered as good fits. b) MC simulation for $J_2/J_1 = 0.9$ and strong local field $h = 2.5$ for 100 and 120 nm gap (only copy a and b were used for 120 nm gap). One can see that the ground state favours type III and type IV lattices. c) MC simulation for $J_2/J_1 = 0.8$ and $h = 1.5$ for 140, 160, 180, 200, 220, 240, 260 and 280 nm gap.

To favour the type III and type IV tiling, a local alternating magnetic field h can be implemented in the Hamiltonian. The field alternates on the vertex sites forcing the formation of all-in/all-out vertex type. The system with the J_1 and J_2 coupling and this local magnetic field h can be described by the Hamiltonian $\mathcal{H}_h$

$$\mathcal{H}_h = \mathcal{H} - h\sum_k \sigma_k = -\frac{1}{2}\sum_{\langle\langle ij\rangle\rangle} J_{ij}\sigma_i\sigma_j - h\sum_k \sigma_k, \tag{4.1}$$

where the new summation coefficient k sums over all sites in the system. The original Hamiltonian $\mathcal{H}$ is defined by equation 2.1.

In figure 4.7a can be seen similar heatmap as in figure 4.5 for which the same threshold value was set (i.e. $5 \cdot 10^{-4}$). In this case, simulations for different J_2/J_1 ratios and h values were done (i.e. additional 63 simulations). Determining only one set of parameters for each lattice is even more complicated than for the previous set of simulations. However, for small gaps (100 and 120 nm gap) one can see a series of fits with decent accuracy. The MC simulation that fits very well for small lattices was set for parameters $J_2/J_1 = 0.9$ and $h = 2.5$ (see figure 4.7b). This is thanks to the h parameter which was missing in the previous set of simulations. The strong local field is important for the lattices with small gaps and the J_2/J_1 ratio is less significant, but for lattices with larger gaps the importance of the J_2/J_1 ratio grows and the local field h value is smaller. To prove that, one can see the area of yellow cells (i.e. bad fit accuracy) for gaps larger than 120 nm and h value larger than 2, or in figure 4.7c can be seen MC simulation for parameters $J_2/J_1 = 0.8$ and $h = 1.5$ were vertex populations fit very well. Also, more lattices fit on one MC simulation with the h parameter included than for the simulations without the h parameter (i.e. for $h = 0$).
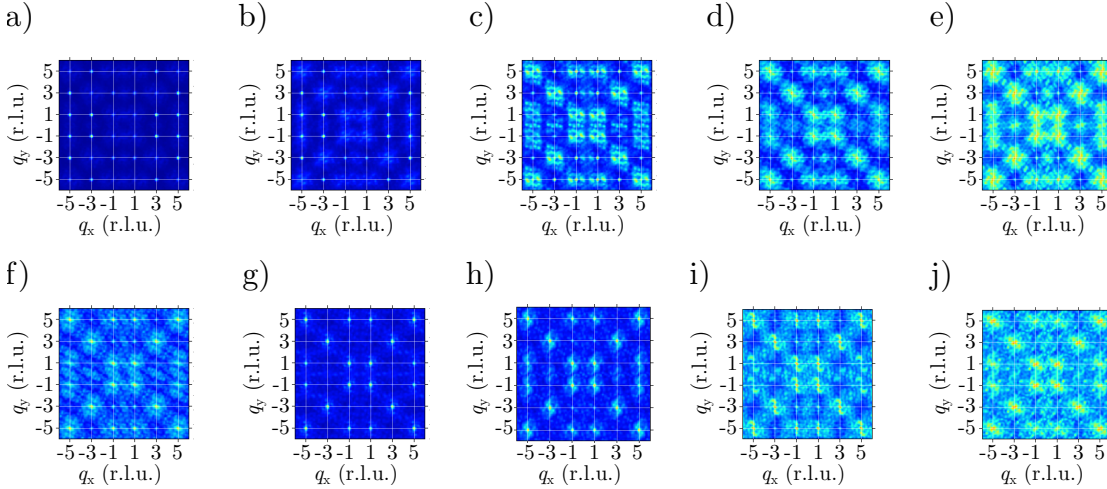

Fig. 4.8: Computed averaged magnetic structure factors for each gap. For each gap, three MSF were averaged (copy a, b and c). Magnetic structure factors a)–j) correspond to gaps 100 to 280 nm.

As was mentioned above for determining the right model one needs to analyse the MSF results as well. In figure 4.8 are presented averaged MSF for each gap. The MSF for small gaps (100 and 120 nm) are different than the MSF for larger gaps. In figure 4.8a and 4.8b the Bragg peaks representing the type I tiling (see illustrating figure 3.7) are missing and emerge for larger gaps. On the contrary, Bragg peaks

associated with type III and type IV tiling are present in every MSF except figures 4.8g and 4.8j. Also, for the smallest gaps (see figures 4.8a and 4.8b) the type III and type IV Bragg peaks are the most intense. This supports the importance of the h parameter in MC simulations and its large value that favors the type III tiling. Besides the Bragg peaks, one can see the faint background that emerges with a gradually increasing gap to its most intense state in figure 4.8e.
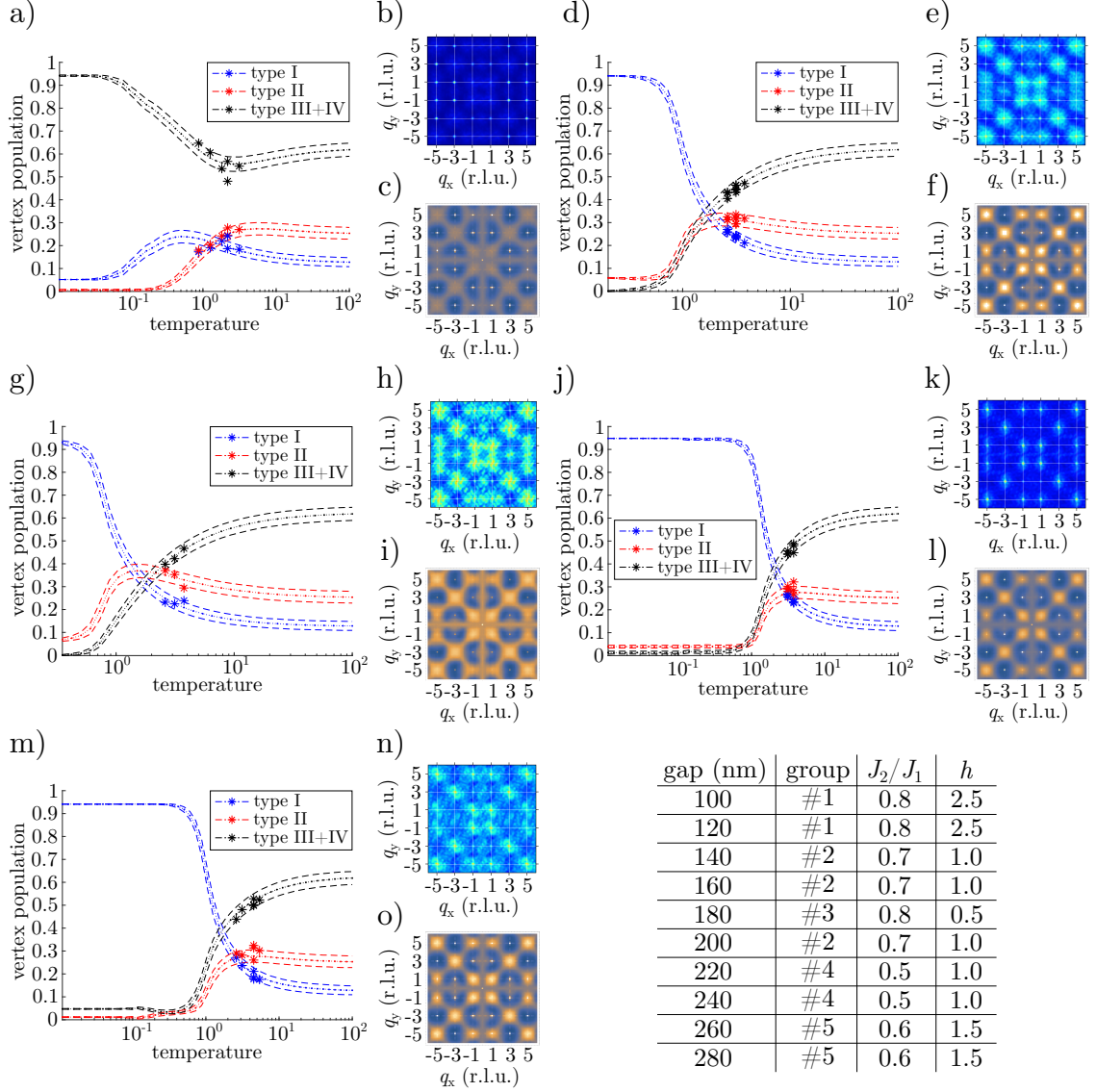

Fig. 4.9: Population curves with experimental MSF and simulated MSF by Monte Carlo for five groups. In subfigures a), d), g), j) and m) are population curves that were calculated for J_2/J_1 and h parameters noted in the table. In subfigures b), e), h), k) and n) are experimental MSF averaged over all measurements present in the group. In subfigures c), f), i), l) and o) are MSF calculated for the same group parameters.

gap (nm)	group	J_2/J_1	h
100	#1	0.8	2.5
120	#1	0.8	2.5
140	#2	0.7	1.0
160	#2	0.7	1.0
180	#3	0.8	0.5
200	#2	0.7	1.0
220	#4	0.5	1.0
240	#4	0.5	1.0
260	#5	0.6	1.5
280	#5	0.6	1.5

Comparing the experimental results and MC simulations of MSF for parameters provided by the fitting accuracy (see figure 4.7a) an agreement between experimen-

tal and theoretical MSF can be found. To analyse the experimental MSF a division into several groups is more appropriate. By analysing the MSF in figure 4.8, measurements were divided into five groups. Group #1 consists of lattices with 100 and 120 nm gaps. This group is characteristic of type III and type IV tiling Bragg peaks in MSF (see figures 4.8a–b) and a tendency for higher h values in the MC simulations (see figure 4.7a). Group #2 consists of lattices with 140, 160 and 200 nm gaps. In this group, one can see emerging type I tiling (see figures 4.8c–d and 4.8f). The behaviour of lattices with a 180 nm gap is slightly different and deserves a unique group #3. For larger gaps, Bragg peaks for type I tiling are becoming more narrow thus lattices with 220 and 240 nm gaps are examined in group #4 (see figures 4.8g–h). The last group #5 contains lattices with 260 and 280 nm gaps. There the Bragg peaks tend to be wider once again (see figures 4.8i–j).

In figure 4.9 can be seen MC simulation curves and MC simulation of MSF for the same parameters J_2/J_1 and h with corresponding experimental averaged MSF for all five groups described above. These results fulfil both conditions necessary for the right description of the system, i.e. the vertex population fractions and the correlations encrypted in the MSF. By a simple comparison of simulated MSF for the temperature windows obtained from the vertex population MC simulations and experimental MSF can be concluded that the model explains the experimental results for small and large gaps very well and also can be used as a far better description of the 180 nm gap lattices than a "spin liquid" model provided so far.

This new set of MSF has the important type III and type IV Bragg peaks at the exact locations as the experiment one. In figure 4.9b the faint background is emerging in the same way as in the experimental MSF in figure 4.9c. For larger gaps, wider and unconnected Bragg peaks linked with type I tiling are also visible. In group #3 the comparison between the MSFs is also very good except for the not sufficient drop of intensity for $q_x = 0$ and $q_y = 0$ coordinates in the simulated MSF. To have an even better match with the model a slight increase of the intensity in between the central Bragg peaks at $[q_x, q_y] = [\pm 1, 0]$ and $[0, \pm 1]$ coordinates would be needed to form the intensity ring in donut shape as can be seen in figure 4.9i. For the largest gaps in groups #4 and #5 the accuracy of population curves fitting and the MSFs are again in good agreement.

After the successful determination of a more accurate model, it would be interesting to examine the specific behaviour of type III vertices in other lattices and make sure that the tiling of type III and type IV is observable in the same sense as in figures 4.2b and 4.3b.

4.3.3 The behaviour of the lattices with small gaps

In the first spin configurations shown in this work, the surprising clustering of type III vertices was clearly visible. From the beginning, there was an effort to reduce the number of excitations in the system (type III and type IV vertices) and reach the predicted spin liquid phase. However, observation of this state is more difficult than expected, and types III and types IV vertices were still occurring.

It is therefore interesting to focus more on the lattices where type III and type IV vertices are dominant. The population curves after the mapping (see figure 4.4b) indicates a rapid increase of type III vertices for the smallest gaps (i.e. 100 nm

and 120 nm gaps). Also, the MSFs predict type III tiling for the same lattices (see figure 4.9c) and a large h value derived from MC simulation supports the selection of lattices with small gaps.
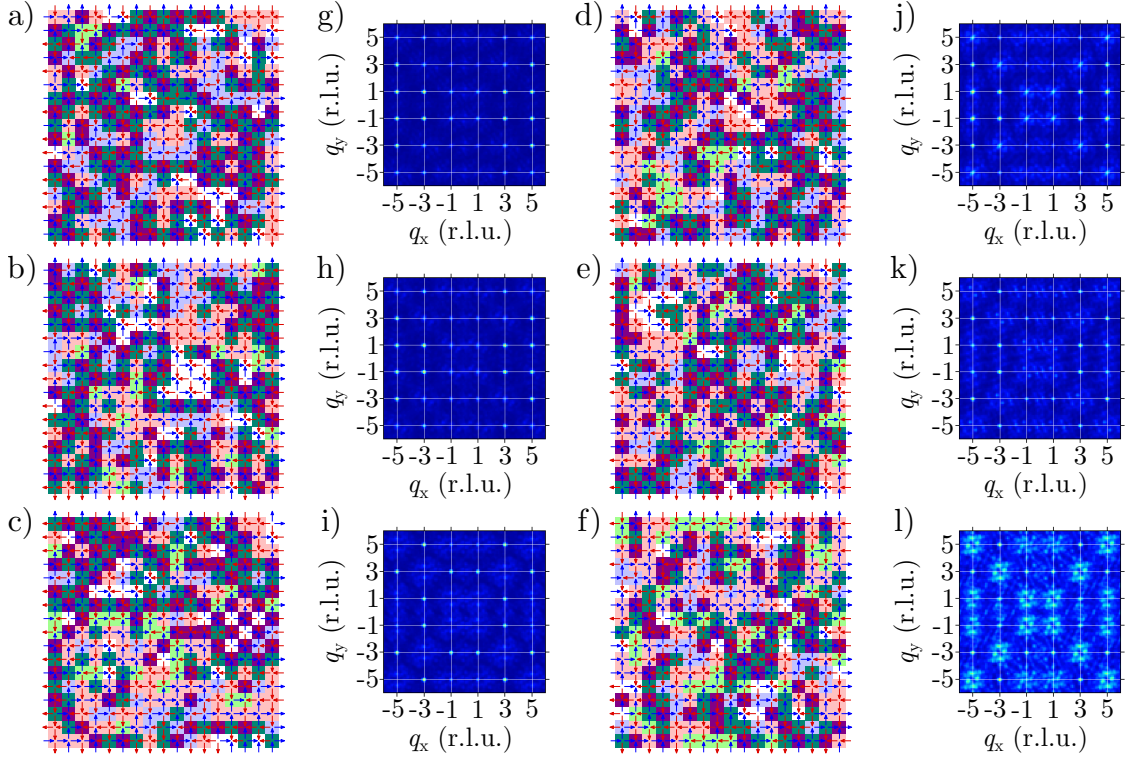

Fig. 4.10: Spin configurations for lattices with 100 nm gap a)–c) and for lattices with 120 nm gap d)–f). g)–l) Magnetic structure factors for corresponding a)–f) spin configurations. In a) the charge crystallisation of type III vertices is clearly visible. MSFs have sharp Bragg peaks at the q-vectors indicating type III tiling.

In figure 4.10 can be seen spin configurations for lattices with 100 nm and 120 nm gaps. For all spin configurations with the smallest gap, the type III clustering and charge crystallisation (chessboard arrangement made by violet and dark green vertices) extends throughout the whole lattice (see figure 4.10a). In each of the MSFs, the faint background is visible showing the subtle presence of type I and type II. The stronger presence of this background is visible in figure 4.10l where the number of excitations is reduced and type I and type II vertices are increasing their populations. It suggests that under some circumstances the shakti lattice can be mapped to a system where the ground state is formed by type III (or type IV) vertices with crystallised charges. To prove these assumptions further research going beyond this work is needed.

4.4 Energies of mapped vertices

By nature of the new mapping definition, the energy hierarchy of the vertices after the mapping is different than the classical one described in section 2.3.1. In the

original definition for only type I and type II vertices, there was no problem with multiple vertex energies. Each of the possible spin configurations had always two C_1 vertices and two C_2 vertices. Type III after the mapping is defined as a plaquette with three C_1 vertices and one C_2 vertex or a plaquette with one C_1 vertex and three C_2 vertices. Because of these two possible configurations, two groups of type III energies are present (see section 2.5.2). Plaquettes with more type C_1 (resp. C_2) at T junction vertices than with C_2 (resp. C_1) at T junction vertices are named type III_{C_1} (resp. type III_{C_2}) vertices. The same problem occurs with type IV. Depending on the number of type C_1 or C_2 at T junctions type IV_{C_1} and type IV_{C_2} is defined.

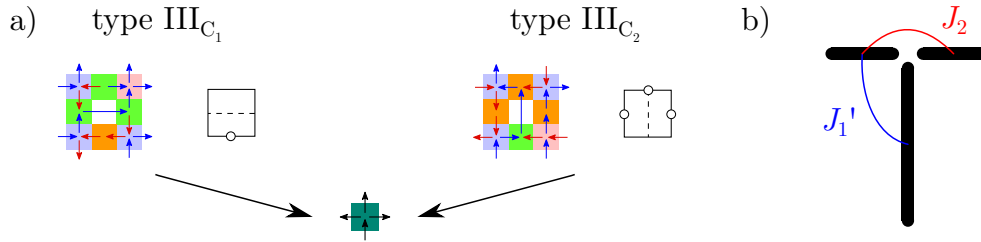Fig. 4.11: a) Examples of two spin configurations in the shakti lattice for type III_{C_1} and type III_{C_2}. Even with different spin configurations in the shakti lattice, the plaquette is projected to an identical type III vertex. b) Interactions between first (J_1') and second (J_2) neighbours at the T junction.

In figure 4.11a can be seen two different spin configurations that yield the same result after the mapping. When the shakti lattice is mapped to the square lattice, part of the information is lost. Because of the presence of other vertex types different than type T_1 at the cross vertices, reverse mapping is no longer possible. To calculate the energy of the plaquette before the mapping, the energy of the T junction for each vertex type must be defined. These energies can be calculated by equations 4.2–4.4.

$$E_{C_1} = -2J_1' + J_2, \qquad (4.2)$$

$$E_{C_2} = -J_2, \qquad (4.3)$$

$$E_{C_3} = +2J_1' + J_2. \qquad (4.4)$$

In these equations, the J_2 coupling strength of the second neighbours is the same as for nano-magnets interacting in the CSL lattice (see section 2.3). Due to the fact that the long island nano-magnet has different dimensions, the coupling strength between the long island nano-magnet and the closest short nano-magnet would not be the same as in the CSL lattice. To distinguish between these two couplings for the T junction, the coupling strength between the first neighbours will be J_1'.

Now let's compare the energies of type III_{C_1} and type III_{C_2}. This simply means to sum all T junction energies in each plaquette. For the type III_{C_1} vertex the energy of T junctions is $-6J_1' + 2J_2$ but for the type III_{C_2} it is $-2J_1' - 2J_2$. This proves that two groups of vertices in an excited state exist in the system and to understand the shakti system from an energetical point of view this must be taken into account.

This favouring of one type over another one can be seen in figure 4.1b where the population of T junction vertices is plotted on the gap dependence.

4.4.1 Effect of the corners

To completely describe the energy of mapped vertices one must include the corners of the plaquette. It is obvious that a plaquette with one type T_1, two types T_2 and one type T_3 at the corner would be more energy-demanding than a plaquette with only one type T_2 and three types T_1. Because the definition of mapping is done by T junction vertices these nuances at the corners are not transcribed into the spin configuration after the mapping. The schematic of this second type of information loss is shown in figure 4.12.
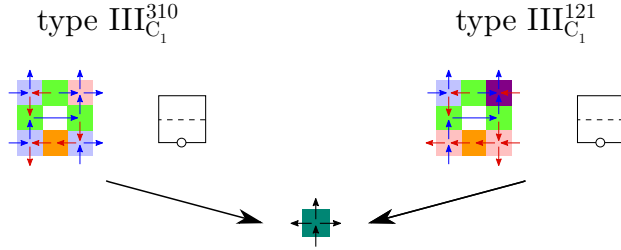

Fig. 4.12: Example of plaquettes in the shakti lattice for type $\mathrm{III}_{\mathrm{C}_1}$ with different plaquette corners. The three digits mean the number of type T_1, type T_2 and type T_3 vertices present at the corners. After the conversion to the circle notation (or spin notation after the mapping), this information is lost.

To express the configuration of corners in the shakti plaquette, three digits are used. The first digit gives the number of type T_1 vertices, the second digit the number of type T_2 vertices and the last digit gives the number of type T_3 vertices. To cover all possible configurations, even the type T_4 should be taken into account. However, the presence of type T_4 cross vertex is very close to zero after the demagnetisation protocol, it is therefore fine to neglect this possibility. Because there are four corner cross vertices present in the shakti plaquette, the sum of these three digits must be always equal to 4. This yields that there are 14 possible compositions for type $\mathrm{III}_{\mathrm{C}_1}$ and 14 possible compositions for type $\mathrm{III}_{\mathrm{C}_2}$. To fulfil the rule 2, at least one type T_2 or type T_3 must be in the shakti plaquette. This implies that type $\mathrm{III}_{\mathrm{C}_1}^{400}$ vertex is not possible and type $\mathrm{III}_{\mathrm{C}_1}^{310}$ is the candidate for the lowest energy composition. To calculate the energy of the shakti plaquette, the energy of corner cross vertices and the energy of T junction vertices must be summed together. To distinguish between the energy of type III and type IV, the E will describe the energy of type III vertices and the U will describe the energy of type IV vertices.

$$E_{\mathrm{C}_1}^{xyz} = 3E_{\mathrm{C}_1} + E_{\mathrm{C}_2} + x \cdot E_{\mathrm{I}} + y \cdot E_{\mathrm{II}} + z \cdot E_{\mathrm{III}}, \tag{4.5}$$

$$E_{\mathrm{C}_2}^{xyz} = E_{\mathrm{C}_1} + 3E_{\mathrm{C}_2} + x \cdot E_{\mathrm{I}} + y \cdot E_{\mathrm{II}} + z \cdot E_{\mathrm{III}}, \tag{4.6}$$

$$U_{\mathrm{C}_1}^{xyz} = 4E_{\mathrm{C}_1} + x \cdot E_{\mathrm{I}} + y \cdot E_{\mathrm{II}} + z \cdot E_{\mathrm{III}}, \tag{4.7}$$

$$U_{\mathrm{C}_2}^{xyz} = 4E_{\mathrm{C}_2} + x \cdot E_{\mathrm{I}} + y \cdot E_{\mathrm{II}} + z \cdot E_{\mathrm{III}}. \tag{4.8}$$

Equations 4.5 and 4.6 serve as a guide for calculating any of the 14 possible energies. Variables x, y and z stands for the number of type T_1, type T_2 and type T_3 respectively. Equations 4.7 and 4.8 serve as a guide for calculating any of the 12 possible energies for type IV_{C_1} or any of the 15 possible energies for type IV_{C_2} (reason for this number of possibilities is explained in section 4.4.2). The energies of E_{C_1} and E_{C_1} are presented in equations 4.2 and 4.3. The energies of type T_1, type T_2 and type T_3 are the same as presented in equations 2.2–2.4.

In the previous sections, the populations of type III and type IV vertices were merged together. One reason why one can do this is the interesting fact that when the energy of type III_{C_1} and type III_{C_2} is averaged, the energy is the same as for the averaged type IV_{C_1} and type IV_{C_2}. For instance in equation 4.9 can be seen this equivalence for the situation with corners containing two type T_1 and two type T_2.

$$(E_{C_1}^{220} + E_{C_2}^{220})/2 = (U_{C_1}^{220} + U_{C_2}^{220})/2 = -8J_1 - 4J_1'. \tag{4.9}$$

4.4.2 The composition of type III and type IV vertices

When one has the theoretical description of the vertex energies, it is not difficult to plot the "energy ladder" that depends on the ratio of the strength of the second and the first neighbour in the shakti lattice J_2/J_1. This hierarchy can be seen in figure 4.13 where only low energy vertices out of the 28 are shown.
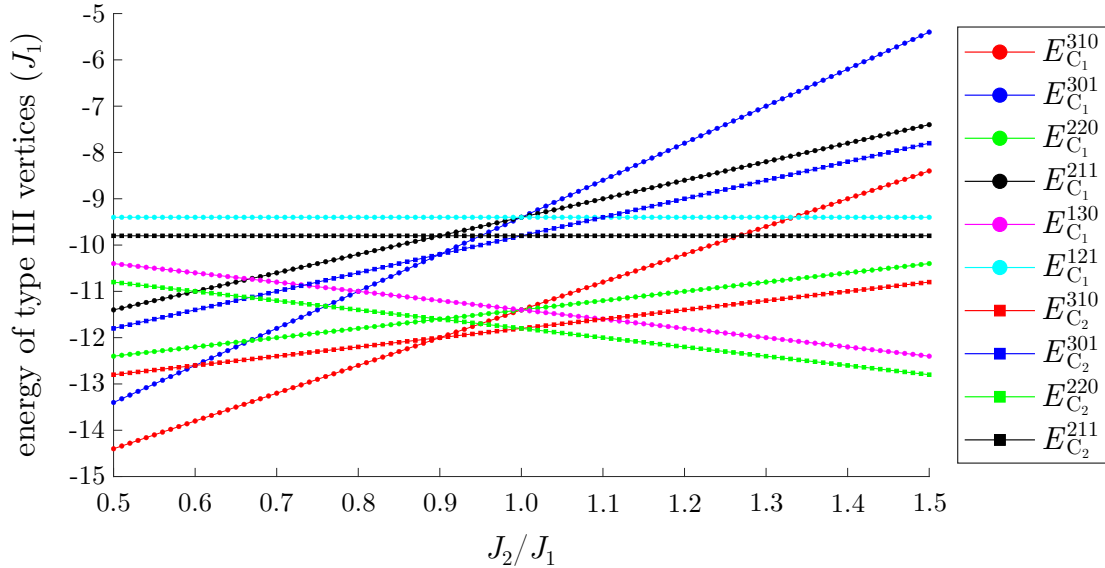

Fig. 4.13: Calculated energy spectrum for type III_{C_1} and type III_{C_2} vertices. The energy of a vertex type depends on the J_2/J_1 ratio. The J_1' value affects the mutual hierarchy of type III_{C_1} and type III_{C_2}. For this computation, the J_1' value is set to $J_1' = 0.9J_1$.

Thanks to this plot one can easily compare the vertex energies of type III for an arbitrary J_2/J_1 ratio. Also, from figure 4.13, it is obvious that the vertex type with the lowest energy is not just one but by tuning the J_2/J_1 ratio one can favour

different low energy type III vertices. This change is occurring for not just the lowest vertex energy but it also holds for the whole energy ladder.

It is natural to expect that type III vertices with the lowest energies should be represented in larger numbers than the vertices with high energies. This can be checked by computing the population of the type III vertices depending on their composition of the corner cross vertices and the T junction vertices. These results can be seen in figure 4.14 where only relevant population curves are shown (vertices with a population lower than 5 % are omitted).
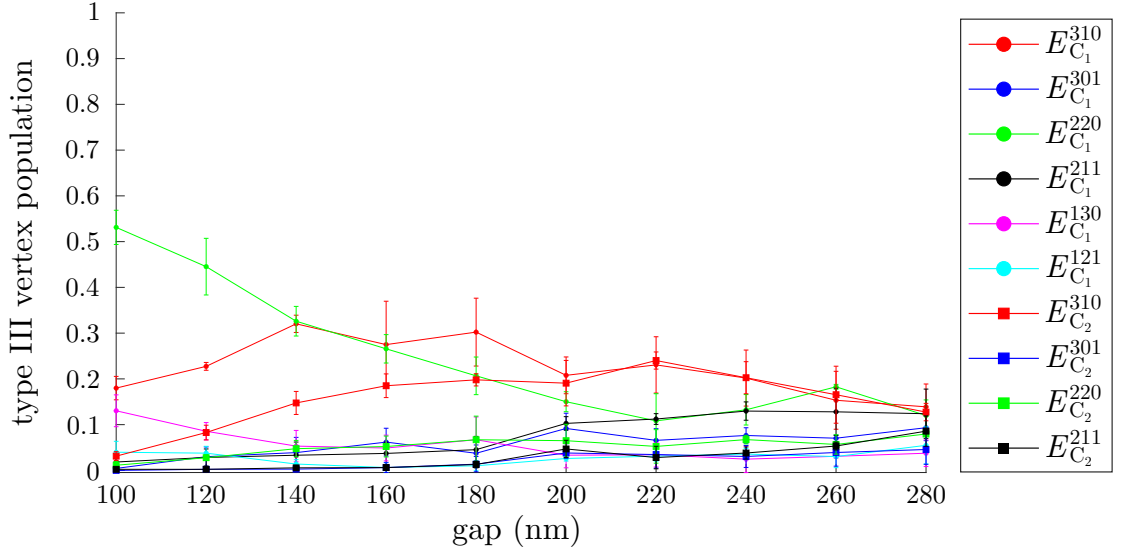
Fig. 4.14: Experimental population curves for different type III_{C_1} and type III_{C_2} vertex compositions dependent on the gap. The markers used in this plot are the same as those used in the theoretical energy spectrum in figure 4.13. Vertices with a population lower than 5 % are omitted.

In figure 4.14 can be seen population curves for 10 different compositions of type III vertices. Populations for each gap were again averaged over three identical lattices. Several interesting results can be made from the experimental data. The most frequent vertex compositions are types $III_{C_1}^{220}$, $III_{C_1}^{310}$ and $III_{C_2}^{310}$. These three vertex compositions also appear on the three lowest energy levels in figure 4.13.

It is clear that vertices want to minimise the energy of the system and prefer the compositions with the lowest energy. For lattices with a larger gap than 180 nm, one can even see that type $III_{C_1}^{310}$ is more represented than type $III_{C_2}^{310}$ (or are equally represented) and population with the composition of type $III_{C_1}^{220}$ is decreasing and is lower than the later two. For that region, the interval of J_2/J_1 ratio can be determined so that $J_2/J_1 < 0.9$ (see figure 4.13).

This method of explanation slightly spoils the composition population for the smallest gaps where type $III_{C_1}^{220}$ is represented by almost 50 %. In figure 4.13, there is not an interval where type $III_{C_1}^{220}$ would have the lowest energy. This substantial increase of the vertex composition can be explained by the large population of type T_2 which is then imprinted into the type III vertices (see the population curve for type T_2 in figure 4.1a for 100 nm and 120 nm gaps).

The reason to investigate the vertex compositions is valid because from figure 4.14, it is obvious that some configurations are more frequent and thus more energetically favourable than others. To understand the dynamics of type III clustering and other phenomena, the understanding of the formation of a plaquette is crucial. For the smallest gaps, the reason for forming the type $III_{C_1}^{220}$ composition is also in the sharing of defects (i.e. types T_2 in the corners of the plaquette) and does not depend only on the energy of a single vertex type.
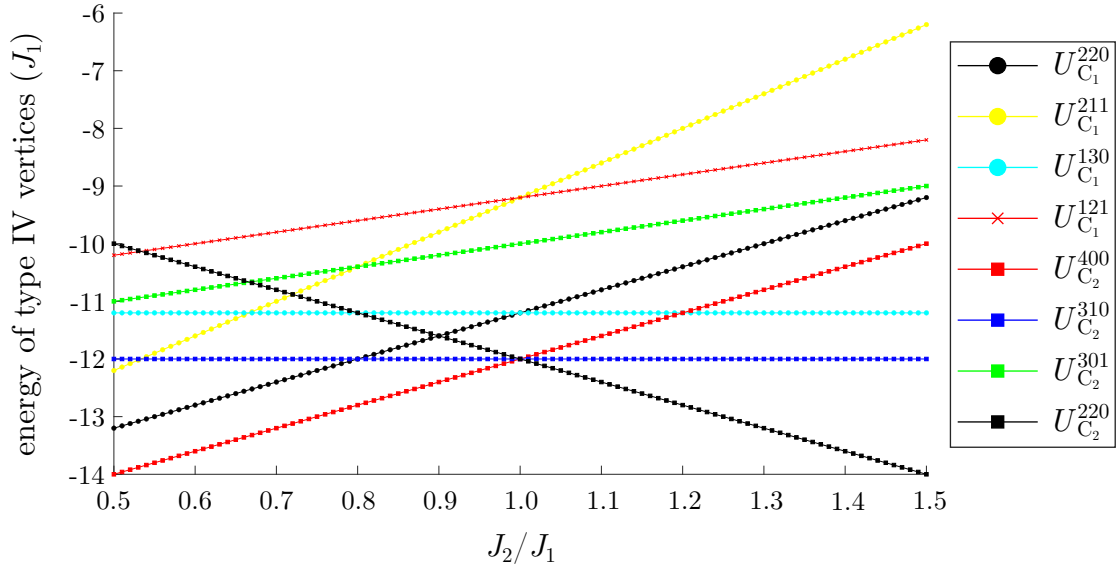
Fig. 4.15: Computed energy spectrum for type IV_{C_1} and type IV_{C_2} vertices. The energy of a vertex type depends on the J_2/J_1 ratio. The J_1' value affects the mutual hierarchy of type IV_{C_1} and type IV_{C_2}. For this computation, the J_1' value is set to $J_1' = 0.9J_1$.

The same analysis of the composition of type III vertices can be made for type IV vertices. For the calculation of the energy spectrum for type IV vertices the equations 4.7 and 4.8 were used. The results of these computations can be seen in figure 4.15. One can notice that the energies for type $IV_{C_1}^{310}$ and type $IV_{C_1}^{301}$ are not present. This is caused by the four C_1 type vertices at all T junctions. This leads to the presence of at least two antiferromagnetic spin corners (e.g. two types T_2 or one type T_2 and one type T_3, etc.) to fulfil the rule 3 described in section 2.5.2. On the other hand, type IV_{C_2} vertices do not have strictly given direction for the two short nano-magnets, thus enabling the type $IV_{C_2}^{310}$ and type $IV_{C_2}^{301}$ and even type $IV_{C_2}^{400}$.

It is not surprising that the lowest energy is for type $IV_{C_2}^{400}$ because of enabling four type T_1 vertices. This dramatically decreases the energy of the plaquette for $J_2/J_1 < 1$. Except for the later composition, type $IV_{C_1}^{220}$, type $IV_{C_2}^{310}$ and type $IV_{C_2}^{220}$ are the vertex compositions with the lowest energy for the J_2/J_1 ratio lower then 1. Now, one can compare the theoretical energy ladder for type IV vertices with experimental data.

In figure 4.16 can be seen the population curves for different type IV compositions depending on the gap of the lattice. For lattices with a gap larger than 140 nm, the composition of type $IV_{C_2}^{400}$ is dominating. This agrees with the same J_2/J_1

interval predicted by the configuration for type III vertices. The second most frequent composition of type IV is the type $\text{IV}_{\text{C}_2}^{310}$ (this again matches for $J_2/J_1 < 1$). For the lattices with small gaps (i.e. 100 nm and 120 nm gap) the behaviour is different. Vertex compositions with a higher fraction of T_2 vertices (type $\text{IV}_{\text{C}_1}^{130}$, type $\text{IV}_{\text{C}_1}^{220}$ and type $\text{IV}_{\text{C}_1}^{121}$) are present because of the shared type T_2 cross vertices.
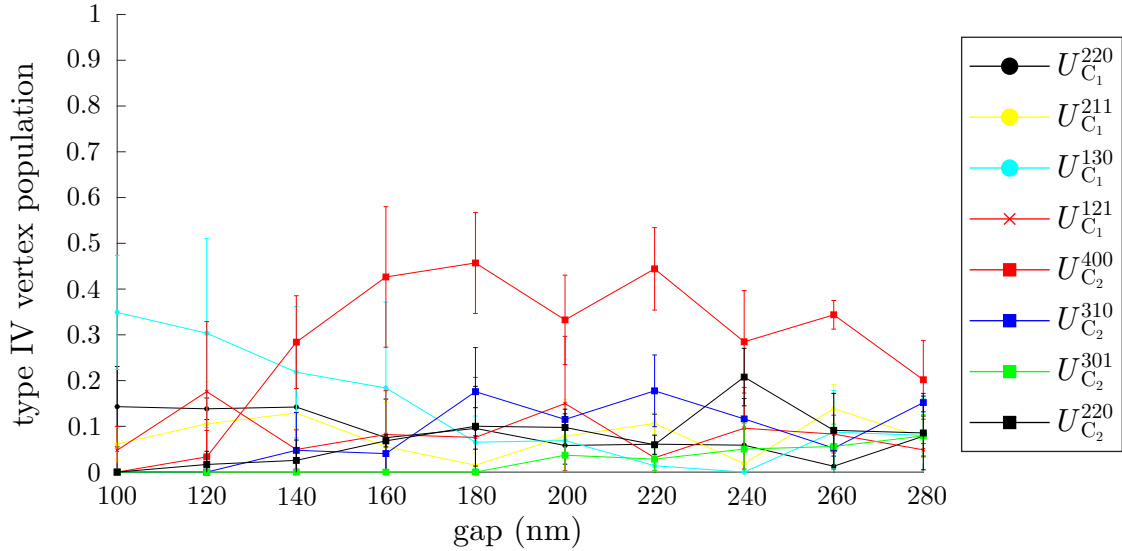
Fig. 4.16: Experimental population curves for different type IV_{C_1} and type IV_{C_2} vertex compositions dependent on the gap. The markers used in this plot are the same as those used in the theoretical energy spectrum in figure 4.15. Vertices with a population lower than 5 % are omitted.

This section demonstrated the complex behaviour of the shakti lattice system and reminds the fact that some information is lost in the process of extended mapping presented in this work. It is important to include in any future works about the shakti system the fact that vertices after the mapping do not have the same energy as would be expected in the classical 16 vertex model. This was proved by the analysis of the theoretical energies of single vertices (see figures 4.13 and 4.15) and by observing the same phenomena experimentally (see figures 4.14 and 4.16).

5 Conlusion

This work focused on the artificial spin system with the shakti geometry. I showed how its physics can be mapped to the one of the square geometry. To interpret the results, the mapping definition was extended to include type III and type IV vertices which behave like electrostatically charged quasi-particles in the square ice.

By measuring several shakti lattices with MFM for a wide range of gaps, good statistics was provided to analyse the behaviour of the shakti system. The vertex populations and configurations in reciprocal space provided by MSF were used for the analysis. The use of the MSF enables to analyse the magnetic correlations in the system.

The lattices with the highest fraction of type T_1 at the cross vertices were natural candidates for the observation of the predicted spin liquid phase for the system mapped to the square lattice. After analysing my experiments and experiments provided in the literature, an important conclusion was made. The shakti system with the population of type T_1 around 85 % is not sufficient to exhibit the signatures of the disordered spin liquid phase. This means that my measurements could not reach the shakti ice physics. Also, the presence of type III and type IV vertices can not be associated with the monopole-like behaviour of excitations in the Coulomb phase. Surprised by these results and the essential differences between the experimental results and theoretical predictions led to an effort to find a new model that would better describe the shakti system.

For finding the new model, Monte Carlo simulations were used. The procedure to find a better model was done by fitting the vertex populations obtained from the experiments on the population curves computed by Monte Carlo simulations. To be sure that spin correlations are the same in the experiments and that the new model describes them as well, a comparison of the MSF calculated from the experiments and simulated by Monte Carlo was done. The new model consists of two variable parameters. The J_2/J_1 parameter affects the composition of the background formed by type T_1 and type T_2 vertices. For the shakti ice, it should be equal to one, but experimental results can not reach such a condition, and this parameter was lower than one for all my measurements. The h parameter is the second parameter and describes a local alternating field on each vertex, which favours the configuration of type III and type IV vertices that are inherently present in the shakti system with the population of type T_1 at the cross vertices lower than 100 %.

After the analysis of the experiments, it was observed that by changing the gap between the nano-magnets in the shakti lattice, the system after the mapping is characterized by different parameters. By tuning the gap parameter one can choose different models. For gaps similar to the width of the nano-magnets, the effect of charge crystallisation is visible, and type III and type IV tiling emerges (i.e. h is larger). Lattices with larger gaps tend to be described by smaller h parameters. MSFs of these lattices have a typical shape of wide Bragg peaks at the same q-vectors as the MSF background for 100 nm and 120 nm gaps. This new model includes the specific behaviour of type III and type IV vertices especially for small gaps that were not taken into account in the previous model.

To understand the dynamics of the charge crystallisation and type III and type

IV tiling, the energy hierarchy of the excitations was studied. During the mapping process, some information is lost due to the mapping procedure. This information is stored in the composition of the plaquettes that are mapped to the vertices in the square lattice. The compositions of type III and type IV plaquettes were studied both theoretically and experimentally. The experiments confirmed that several energies are associated with one vertex type after the mapping and that the formation of type III clusters is driven by the plaquette composition.

This work extended the understanding of the artificial shakti system and helped to get insight into the physics of the shakti lattice. However, the observation of the pure spin liquid phase or Coulomb phase is experimentally very difficult. Otherwise, this work can serve as an inspiration for studying the fascinating charge crystallisation effect.

Bibliography

[1] Rodney J. Baxter. *Exactly solved models in statistical mechanics*. London ; New York: Academic Press, 1982.

[2] J. D. Bernal and R. H. Fowler. "A Theory of Water and Ionic Solution, with Particular Reference to Hydrogen and Hydroxyl Ions". in: *The Journal of Chemical Physics* 1.8 (Aug. 1933), pp. 515–548. DOI: 10.1063/1.1749327.

[3] G. Binnig, C. F. Quate, and Ch. Gerber. "Atomic Force Microscope". in: *Physical Review Letters* 56.9 (Mar. 1986), pp. 930–933. DOI: 10.1103/PhysRevLett. 56.930.

[4] Steven T Bramwell and Mark J Harris. "The history of spin ice". in: *Journal of Physics: Condensed Matter* 32.37 (Sept. 2020), p. 374010. DOI: 10.1088/1361-648X/ab8423.

[5] Steven T. Bramwell, Michel J. P. Gingras, and Peter C. W. Holdsworth. "SPIN ICE". in: *Frustrated Spin Systems*. 2nd ed. WORLD SCIENTIFIC, May 2013, pp. 383–474. DOI: 10.1142/9789814440745_0007.

[6] Ondřej Brunn. "Magnetic phases in an artificial realization of the square ice model". Diploma thesis. Brno University of Technology, 2019.

[7] Zoe Budrikis, Paolo Politi, and R. L. Stamps. "Diversity Enabling Equilibration: Disorder and the Ground State in Artificial Spin Ice". in: *Physical Review Letters* 107.21 (Nov. 2011), p. 217204. DOI: 10.1103/PhysRevLett. 107.217204.

[8] Zoe Budrikis et al. "Disorder Strength and Field-Driven Ground State Domain Formation in Artificial Spin Ice: Experiment, Simulation, and Theory". in: *Physical Review Letters* 109.3 (July 2012), p. 037203. DOI: 10.1103/PhysRevLett.109.037203.

[9] Claudio Castelnovo, Roderich Moessner, and Shivaji L. Sondhi. "Magnetic Monopoles in Spin Ice". in: *Nature* 451.7174 (Jan. 2008), pp. 42–45. DOI: 10.1038/nature06433.

[10] Gia-Wei Chern, Muir J. Morrison, and Cristiano Nisoli. "Degeneracy and Criticality from Emergent Frustration in Artificial Spin Ice". in: *Physical Review Letters* 111.17 (Oct. 2013), p. 177201. DOI: 10.1103/PhysRevLett.111. 177201.

[11] Alan Farhan et al. "Emergent magnetic monopole dynamics in macroscopically degenerate artificial spin ice". in: *Science Advances* 5.2 (Feb. 2019), eaav6380. DOI: 10.1126/sciadv.aav6380.

[12] D. A. Garanin and Benjamin Canals. "Classical spin liquid: Exact solution for the infinite-component antiferromagnetic model on the *kagomé* lattice". in: *Physical Review B* 59.1 (Jan. 1999), pp. 443–456. DOI: 10.1103/PhysRevB. 59.443.

[13] W. F. Giauque and Muriel F. Ashley. "Molecular Rotation in Ice at 10°K. Free Energy of Formation and Entropy of Water". in: *Physical Review* 43.1 (Jan. 1933), pp. 81–82. DOI: 10.1103/PhysRev.43.81.2.

[14] Ian Gilbert et al. "Emergent ice rule and magnetic charge screening from vertex frustration in artificial spin ice". in: *Nature Physics* 10.9 (Sept. 2014), pp. 670–675. DOI: 10.1038/nphys3037.

[15] M. J. Harris et al. "Geometrical Frustration in the Ferromagnetic Pyrochlore Ho 2 Ti 2 O 7". in: *Physical Review Letters* 79.13 (Sept. 1997), pp. 2554–2557. DOI: 10.1103/PhysRevLett.79.2554.

[16] Christopher L. Henley. "The "Coulomb Phase" in Frustrated Systems". in: *Annual Review of Condensed Matter Physics* 1.1 (Aug. 2010), pp. 179–210. DOI: 10.1146/annurev-conmatphys-070909-104138.

[17] Yuyang Lao et al. "Classical topological order in the kinetics of artificial spin ice". in: *Nature Physics* 14.7 (July 2018), pp. 723–727. DOI: 10.1038/s41567-018-0077-0.

[18] Demian Levis. "Two-dimensional Spin Ice and the Sixteen-Vertex Model". PhD thesis. Université Pierre et Marie Curie - Paris VI, Oct. 2012.

[19] Elliott H. Lieb. "Exact Solution of the F Model of An Antiferroelectric". in: *Physical Review Letters* 18.24 (June 1967), pp. 1046–1048. DOI: 10.1103/PhysRevLett.18.1046.

[20] Elliott H. Lieb. "Exact Solution of the Problem of the Entropy of Two-Dimensional Ice". in: *Physical Review Letters* 18.17 (Apr. 1967), pp. 692–694. DOI: 10.1103/PhysRevLett.18.692.

[21] Elliott H. Lieb. "Exact Solution of the Two-Dimensional Slater KDP Model of a Ferroelectric". in: *Physical Review Letters* 19.3 (July 1967), pp. 108–110. DOI: 10.1103/PhysRevLett.19.108.

[22] Elliott H. Lieb. "Residual Entropy of Square Ice". in: *Physical Review* 162.1 (Oct. 1967), pp. 162–172. DOI: 10.1103/PhysRev.162.162.

[23] Y. Martin and H. K. Wickramasinghe. "Magnetic imaging by "force microscopy" with 1000 Å resolution". in: *Applied Physics Letters* 50.20 (May 1987), pp. 1455–1457. DOI: 10.1063/1.97800.

[24] R. Moessner, Oleg Tchernyshyov, and S. L. Sondhi. "Planar Pyrochlore, Quantum Ice and Sliding Ice". in: *Journal of Statistical Physics* 116.1 (Aug. 2004), pp. 755–772. DOI: 10.1023/B:JOSS.0000037247.54022.62.

[25] Jason P. Morgan et al. "Thermal ground-state ordering and elementary excitations in artificial magnetic square ice". in: *Nature Physics* 7.1 (Jan. 2011), pp. 75–79. DOI: 10.1038/nphys1853.

[26] Muir J Morrison, Tammie R Nelson, and Cristiano Nisoli. "Unhappy vertices in artificial spin ice: new degeneracies from vertex frustration". in: *New Journal of Physics* 15.4 (Apr. 2013), p. 045009. DOI: 10.1088/1367-2630/15/4/045009.

[27] David Nečas and Petr Klapetek. "Gwyddion: an open-source software for SPM data analysis". in: *Open Physics* 10.1 (Feb. 2012), pp. 181–188. DOI: 10.2478/s11534-011-0096-2.

[28] V.-D. Nguyen et al. "Competing interactions in artificial spin chains". in: *Physical Review B* 96.1 (July 2017), p. 014402. DOI: 10.1103/PhysRevB.96.014402.

[29] Linus Pauling. "The Structure and Entropy of Ice and of Other Crystals with Some Randomness of Atomic Arrangement". in: *Journal of the American Chemical Society* 57.12 (Dec. 1935), pp. 2680–2684. DOI: 10.1021/ja01315a102.

[30] Yann Perrin. "Réseaux artificiels à frustration géométrique". PhD thesis. Université Grenoble Alpes, Oct. 2016.

[31] Yann Perrin, Benjamin Canals, and Nicolas Rougemaille. "Extensive degeneracy, Coulomb phase and magnetic monopoles in artificial square ice". in: *Nature* 540.7633 (Dec. 2016), pp. 410–413. DOI: 10.1038/nature20155.

[32] J M Porro et al. "Exploring thermally induced states in square artificial spin-ice arrays". in: *New Journal of Physics* 15.5 (May 2013), p. 055012. DOI: 10.1088/1367-2630/15/5/055012.

[33] N. Rougemaille and B. Canals. "The magnetic structure factor of the square ice: A phenomenological description". in: *Applied Physics Letters* 118.11 (Mar. 2021), p. 112403. DOI: 10.1063/5.0043520.

[34] Nicolas Rougemaille and Benjamin Canals. "Cooperative magnetic phenomena in artificial spin systems: spin liquids, Coulomb phase and fragmentation of magnetism – a colloquium". in: *The European Physical Journal B* 92.3 (Mar. 2019), p. 62. DOI: 10.1140/epjb/e2018-90346-7.

[35] Franz Rys. "Über ein zweidimensionales klassisches Konfigurationsmodell". in: *Helvetica Physica Acta* 36 (Aug. 1963), pp. 537–559. DOI: 10.5169/SEALS-113387.

[36] Vojtěch Schánilec. "Magnetic spin ice states in artificial magnetic frustrated systems". Diploma thesis. Brno University of Technology, 2018.

[37] Henry Stopfel et al. "Magnetic order and energy-scale hierarchy in artificial spin-ice structures". in: *Physical Review B* 98.1 (July 2018), p. 014435. DOI: 10.1103/PhysRevB.98.014435.

[38] J. Villain. "The 3-dimensional eight vertex model and the proton-proton correlation functions in ice". in: *Solid State Communications* 10.10 (May 1972), pp. 967–970. DOI: 10.1016/0038-1098(72)90232-3.

[39] R. F. Wang et al. "Artificial 'spin ice' in a geometrically frustrated lattice of nanoscale ferromagnetic islands". in: *Nature* 439.7074 (Jan. 2006), pp. 303–306. DOI: 10.1038/nature04447.

[40] Sheng Zhang et al. "Crystallites of magnetic charges in artificial spin ice". in: *Nature* 500.7464 (Aug. 2013), pp. 553–557. DOI: 10.1038/nature12399.